

Performance-Portable Binary Neutron Star Mergers with AthenaK

JACOB FIELDS,^{1,2} HENGRUI ZHU,^{3,4} DAVID RADICE,^{1,5,2,*} JAMES M. STONE,⁶ WILLIAM COOK,⁷ SEBASTIANO BERNUZZI,⁷
AND BORIS DASZUTA⁷

¹*Department of Physics, The Pennsylvania State University, University Park, PA 16802*

²*Institute for Gravitation & the Cosmos, The Pennsylvania State University, University Park, PA 16802*

³*Department of Physics, Princeton University, Jadwin Hall, Washington Road, New Jersey, 08544, USA*

⁴*Princeton Gravity Initiative, Princeton University, Princeton, New Jersey, 08544, USA*

⁵*Department of Astronomy & Astrophysics, The Pennsylvania State University, University Park, PA 16802*

⁶*School of Natural Sciences, Institute for Advanced Study, 1 Einstein Drive, Princeton, NJ 08540, USA*

⁷*Theoretisch-Physikalisches Institut, Friedrich-Schiller-Universität Jena, 07743, Jena, Germany*

(Dated: November 26, 2024)

ABSTRACT

We introduce an extension to the **AthenaK** code for general-relativistic magnetohydrodynamics (GRMHD) in dynamical spacetimes using a 3+1 conservative Eulerian formulation. Like the fixed-spacetime GRMHD solver, we use standard finite-volume methods to evolve the fluid and a constrained transport scheme to preserve the divergence-free constraint for the magnetic field. We also utilize a first-order flux correction (FOFC) scheme to reduce the need for an artificial atmosphere and optionally enforce a maximum principle to improve robustness. We demonstrate the accuracy of **AthenaK** using a set of standard tests in flat and curved spacetimes. Using a SANE accretion disk around a Kerr black hole, we compare the new solver to the existing solver for stationary spacetimes using the so-called “HARM-like” formulation. We find that both formulations converge to similar results. We also include the first published binary neutron star (BNS) mergers performed on graphical processing units (GPUs). Thanks to the FOFC scheme, our BNS mergers maintain a relative error of $\mathcal{O}(10^{-11})$ or better in baryon mass conservation up to collapse. Finally, we perform scaling tests of **AthenaK** on OLCF Frontier, where we show excellent weak scaling of $\geq 80\%$ efficiency up to 32768 GPUs and 74% up to 65536 GPUs for a GRMHD problem in dynamical spacetimes with six levels of mesh refinement. **AthenaK** achieves an order-of-magnitude speedup using GPUs compared to CPUs, demonstrating that it is suitable for performing numerical relativity problems on modern exascale resources.

1. INTRODUCTION

Over the last few decades, numerical relativity (NR) has matured into a robust tool for making accurate quantitative predictions for astrophysical phenomena in the strong-field regime of general relativity. Notable successes include the first detection of gravitational waves (GW150914) and the first observed binary neutron star merger (GW170817), both of which were in excellent agreement with models informed by numerical relativity (Abbott et al. 2016, 2017a). Observational data from GW170817 in particular has further fed back into NR, which has been able to use targeted simulations to place

constraints on the neutron star equation of state (EOS) and other progenitor characteristics (Shibata et al. 2017; Ruiz et al. 2018; Radice et al. 2018; Hinderer et al. 2019).

Nevertheless, current NR codes face a number of challenges going forward. Improvements in existing detectors and proposed next-generation detectors promise unprecedented accuracy in observing gravitational-wave events (Abbott et al. 2017b; Maggiore et al. 2020). However, such improvements will require more accurate waveform models, particularly for BNS systems, which are currently dominated by systematic errors at high signal-to-noise ratios (Pürrer & Haster 2020; Gamba et al. 2021).

We also expect future detectors to be sensitive to the BNS post-merger phase. NR data in this regime exhibits a number of issues, with features such as the merger

jmf6719@psu.edu

* Alfred P. Sloan Fellow

time, peak frequency, and survival time depending heavily on numerical schemes, choice and implementation of microphysics, and resolution (Espino et al. 2023; Zappa et al. 2023).

These demands all point to the need for NR simulations at higher resolutions with more accurate numerical methods and more realistic physics. Some recent efforts include the use of high-order methods (including finite-difference, discontinuous Galerkin methods, and pseudospectral methods where appropriate) (Hilditch et al. 2016; Bugner et al. 2016; Kidder et al. 2017; Most et al. 2019; Tichy et al. 2023; Deppe et al. 2023), more accurate Riemann solvers and treatments of the divergence-free condition (Kiuchi et al. 2022), and more realistic neutrino physics (Foucart et al. 2021; Radice et al. 2022; Izquierdo et al. 2023).

Just as important is implementing new computational algorithms which allow for better parallel scaling and more efficient use of resources. For example, both SpECTRE and GR-Athena++, though very different in implementation, use task-based parallelism to overlap communication and computation (Kidder et al. 2017; Stone et al. 2020; Daszuta et al. 2021; Cook et al. 2023). One more notable example is block-based adaptive mesh refinement (AMR). By dividing the mesh into a series of blocks (typically stored in an octree data structure), mesh refinement is achieved by replacing a single block with eight smaller blocks. Though the need to refine entire blocks (often with a 2:1 size constraint) means that more traditional patch-based AMR approaches are in principle more flexible, block AMR avoids redundant computation and is much simpler to parallelize efficiently. Consequently, block-based codes, such as Dendro-GR (Fernando et al. 2019, 2023) and GR-Athena++ (Stone et al. 2020; Daszuta et al. 2021; Cook et al. 2023; Rashti et al. 2024), typically exhibit excellent scaling properties up to $\mathcal{O}(10^4)$ cores or more, and the simpler remeshing and load-balancing operations mean that in practice their grid refinement compares favorably with the most adaptive patch-based methods (e.g., Clough et al. (2015); Radia et al. (2022)).

Another approach is to use graphical processing units (GPUs). Due to their higher energy efficiency compared to CPUs, many modern supercomputers derive a major portion of their computational power from GPUs. Recently, Dendro-GR showed the ability to accelerate binary black hole calculations with GPUs (Fernando et al. 2022), and the GRaM-X and AsterX codes demonstrated single neutron star evolutions in the EinsteinToolkit with GPUs (Shankar et al. 2023; Kalinani et al. 2024).

One challenge for GPU development is that there exist multiple GPU vendors which each preferentially support

different programming models, such as CUDA and HIP. Furthermore, many new machines still contain significant CPU resources, and many tasks such as debugging and simple testing may be easier to do on a personal laptop or workstation, which may not necessarily have a GPU. This leads to a desire for *performance portability*, or the ability not only to run a piece of software on a wide variety of machine architectures and software stacks but to do so *well*. However, manually rewriting different parts of an application for each supported architecture is time-consuming and error-prone.

A more convenient route to performance portability is to use pre-existing libraries. Though several tools exist for performance portability, the one that we highlight here is the Kokkos C++ framework (Trott et al. 2022). Kokkos is an abstraction layer which hides platform-specific details such as optimal memory layout and launching GPU or OpenMP kernels, enabling developers to write high-performance scientific code once and compile on a variety of architectures with various programming models.

AthenaK¹ is a complete rewrite of the Athena++ code using Kokkos. This paper is the third in a series describing its features and capabilities, with Stone et al. (2024) focusing on its architecture and applications to astrophysical fluids, Zhu et al. (2024) discussing the dynamical spacetime solver and infrastructure for binary black hole (BBH) problems, and this paper discussing an extension which couples GRMHD to dynamical spacetimes. In Section 2, we briefly discuss the GRMHD equations. Section 3 provides an overview of our numerical methods, with particular attention given to our atmosphere treatment and the implementation of a first-order flux correction (FOFC) scheme. We demonstrate the code’s accuracy and robustness in Section 4, including a convergence test with the first published BNS mergers performed on GPUs. Lastly, Section 5 describes the results of our performance and scaling tests, demonstrating AthenaK’s suitability for exascale machines. Lastly, we summarize our work in Section 6 and highlight some potential new NR applications for AthenaK.

Throughout the paper, we follow the standard indexing convention: Latin indices refer to spatial indices, e.g., $i, j, k, \dots = \{1, 2, 3\}$, and Greek indices are space-time indices, e.g., $\mu, \nu, \dots = \{0, 1, 2, 3\}$. We also adopt geometric units such that $G = c = k_B = 1$.

¹ see <https://github.com/IAS-Astrophysics/athenaK>

2. 3+1 RELATIVISTIC MAGNETOHYDRODYNAMICS

The ideal GRMHD equations are described by the following systems of equations:

$$\nabla_\mu (\rho u^\mu) = 0, \quad (1a)$$

$$\nabla_\mu T^{\mu\nu} = 0, \quad (1b)$$

$$\nabla_\mu (*F)^{\mu\nu} = 0, \quad (1c)$$

where the first represents baryon conservation; the second, conservation of stress-energy; and the third, the Gauss-Faraday law. The stress-energy tensor for this system is

$$T^{\mu\nu} = (\rho h + b^2) u^\mu u^\nu + \left(P + \frac{b^2}{2} \right) g^{\mu\nu} - b^\mu b^\nu, \quad (2)$$

for a fluid with rest-mass density ρ , four-velocity u^μ , pressure P , total fluid energy density e , and magnetic field (measured in the comoving frame) b^μ with a space-time metric $g_{\mu\nu}$. We further define the total specific enthalpy $h \equiv (e + P)/\rho$, and we write the dual of the electromagnetic tensor as

$$(*F)^{\mu\nu} = b^\mu u^\nu - b^\nu u^\mu. \quad (3)$$

Like its predecessor, **Athena++**, the standard GRMHD solver in **AthenaK** uses a formulation similar to [Gammie et al. \(2003\)](#) (hereafter referred to as “HARM-like”). By lowering the free index in Eq. 1b, the GRMHD equations take the form

$$\partial_t (\sqrt{-g} \rho u^0) + \partial_j (\sqrt{-g} \rho u^j) = 0, \quad (4a)$$

$$\partial_t (\sqrt{-g} T^0_\mu) + \partial_j (\sqrt{-g} T^j_\mu) = \frac{1}{2} \sqrt{-g} (\partial_\mu g_{\alpha\beta}) T^{\alpha\beta}, \quad (4b)$$

$$\partial_t (\sqrt{-g} \hat{B}^i) + \partial_j (\sqrt{-g} (*F)^{ij}) = 0, \quad (4c)$$

where \hat{B}^i is the magnetic field measured in the coordinate frame (i.e., $\hat{B}^i = (*F)^{i0}$), and $g = \det \mathbf{g}$. The source terms in Eq. 4b vanish for ignorable coordinates, which leads to better conservation of energy in fixed spacetimes. However, this is no longer true in dynamical spacetimes, and the structure of this source term is inconvenient.

To formulate a valid Cauchy problem, the Einstein equations are rewritten via a 3+1 decomposition. In the ADM formulation, the line element $ds^2 \equiv g_{\mu\nu} dx^\mu dx^\nu$ is rewritten as

$$ds^2 = -\alpha^2 dt^2 + \gamma_{ij} (dx^i + \beta^i dt) (dx^j + \beta^j dt), \quad (5)$$

where α is the lapse, β^i is the shift, and γ_{ij} is the metric of a spatial slice Σ_t , whose embedding in spacetime is

described by the extrinsic curvature K_{ij} . While the evolution equations for γ_{ij} and K_{ij} are derived as part of the decomposition, both α and β^i are gauge variables with some amount of freedom in their specification. Consequently, the $\partial_t g_{\alpha\beta}$ source term for T^0_0 in Equation 4b contains $\partial_t \alpha$ and $\partial_t \beta_i$, which cannot be generally eliminated without prior knowledge of the gauge condition.

For problems in dynamical spacetimes, the so-called “Valencia” formulation ([Banyuls et al. 1997](#); [Anton et al. 2006](#)) is a more natural choice for GRMHD. We will provide a brief description of this formalism here, but we advise the reader to consult the literature for a more complete discussion (e.g., [Giacomazzo & Rezzolla \(2007\)](#); [Cook et al. \(2023\)](#)).

We define a set of conserved variables $\mathbf{U} = \{D, S_i, \tau\}$:

$$D = \rho W, \quad (6a)$$

$$S_i = (\rho h W^2 + B^2) v_i - (B^k v_k) B_i, \quad (6b)$$

$$\tau = \rho h W^2 + B^2 - P - \frac{1}{2} \left[(B^k v_k)^2 + \frac{B^2}{W^2} \right] - D, \quad (6c)$$

where v^i is the three-velocity in the Eulerian frame, $W = 1/\sqrt{1-v^2}$ is the Lorentz factor, and $B^i = n_\mu (*F)^{\mu i}$ is the magnetic field in the Eulerian frame. The relationship between b^μ and B^i is summarized as

$$b^0 = \frac{W B^i v_i}{\alpha}, \quad (7a)$$

$$b^i = \frac{B^i + \alpha b^0 u^i}{W}. \quad (7b)$$

For notational ease, we also use the tilde \sim to designate a *densitized* variable $\tilde{A} = \sqrt{\gamma} A$, and we define $\hat{v}^i = u^i/W = v^i - \beta^i/\alpha$ and the total pressure $P_{\text{tot}} = P + b^2/2$. The GRMHD equations then take the form

$$\partial_t \tilde{D} + \partial_j (\alpha \tilde{D} \hat{v}^j) = 0, \quad (8a)$$

$$\partial_t \tilde{S}_i + \partial_j \left(\alpha \tilde{S}_i \hat{v}^j - \alpha b_i \frac{\tilde{B}^j}{W} + \alpha \tilde{P}_{\text{tot}} \delta^j_i \right) = G_i^S(\mathbf{U}), \quad (8b)$$

$$\partial_t \tilde{\tau} + \partial_j \left(\alpha \tilde{\tau} \hat{v}^j - \alpha^2 b^0 \frac{\tilde{B}^j}{W} + \alpha \tilde{P}_{\text{tot}} v^j \right) = G^\tau(\mathbf{U}), \quad (8c)$$

$$\partial_t \tilde{B}^i + \partial_j (\alpha [\tilde{B}^i \hat{v}^j - \tilde{B}^j \hat{v}^i]) = 0, \quad (8d)$$

with the source terms

$$G_i^S(\mathbf{U}) = \frac{1}{2} \alpha \tilde{S}^{jk} \partial_i \gamma_{jk} + \tilde{S}_j \partial_i \beta^j - \tilde{E} \partial_i \alpha, \quad (9a)$$

$$G^\tau(\mathbf{U}) = \alpha K_{ij} \tilde{S}^{ij} - \tilde{S}^i \partial_i \alpha, \quad (9b)$$

where $E \equiv \tau + D$ is the total energy density in the Eulerian frame, and $S_{ij} \equiv T_{ij}$ is the stress tensor. Since $B^i = \alpha \hat{B}^i$, it follows that $\hat{B}^i = \sqrt{-g} \hat{B}^i$, and Eq. 8d is consistent with Eq. 4c. Though we no longer have exact conservation for fixed spacetimes, the troublesome gauge terms in the HARM-like formulation have been eliminated.

3. NUMERICAL METHODS

In this section, we provide an overview of the numerical methods we use for the Valencia GRMHD solver. For an explanation of the refinement structure and methods shared with other modules in AthenaK, we refer the reader to Stone et al. (2024).

3.1. Spacetime Evolution

We evolve the spacetime using the Z4c formulation, which add an additional dynamical field to the Einstein equations to damp constraint violations and allow them to propagate away (Bernuzzi & Hilditch 2010; Hilditch et al. 2013). Details of our implementation are found in Zhu et al. (2024), but we will highlight an important difference between GR-Athena++ and AthenaK which is particularly relevant to GRMHD evolution.

As noted in Daszuta et al. (2021); Cook et al. (2023), the original version of GR-Athena++ evolves the spacetime on vertex-centered (VC) grids. A VC grid is convenient for spacetime evolution on adaptive grids because the restriction operation is exact and prolongation is only required for half the points. However, when coupled with a cell-centered (CC) fluid scheme (as is typical for finite-volume schemes), the ADM variables must be interpolated to cell centers for GRMHD calculations, and the matter source terms must be interpolated to vertices for the Z4c equations. Alternatively, one may use a CC spacetime so that the Z4c and GRMHD variables exist at the same points, but both restriction and prolongation then require high-order interpolation operations at all boundary points. Daszuta et al. (2024) introduced support for CC spacetimes to GR-Athena++ and performed a detailed comparison between VC and CC schemes. Though both representations have comparable accuracy, CC spacetimes offer noticeably improved performance for GRMHD problems thanks to the lack of intergrid interpolation. Because of this computational benefit and their simpler implementation, we have chosen to support only CC spacetimes in AthenaK.

3.2. GRMHD Evolution

We use the method of lines and standard high-resolution shock-capturing (HRSC) methods with the Valencia solver in AthenaK. We implement both a local Lax-Friedrichs (LLF) scheme and the Harten-Lax-van Leer-Einfeldt (HLLC) approximate Riemann solver

(Harten et al. 1983; Einfeldt et al. 1991). Though these methods are diffusive, they are computationally efficient, guarantee positivity when coupled with an appropriate reconstruction method, and do not typically produce unphysical results. For reconstruction algorithms, AthenaK includes options for donor-cell reconstruction (i.e., no reconstruction or piecewise-constant reconstruction); a piecewise-linear method (PLM) with a van Leer monotized slope limiter (van Leer 1974); two variants of the piecewise-parabolic method, including the classic method (Colella & Woodward 1984) and a newer variant with an extrema-preserving limiter (Colella & Sekora 2008), which we refer to as PPM4 and PPMX, respectively; and a fifth-order weighted essentially non-oscillatory scheme using the Z smoothness indicator (WENOZ) (Borges et al. 2008). We treat ρ , Wv^i , and P as our primitive variables for reconstruction. To preserve the divergence-free constraint, $\partial_i \hat{B}^i = 0$, AthenaK uses the same upwind constrained transport scheme as Athena++ (Gardiner & Stone 2005, 2008; Stone et al. 2020). AthenaK has several time integrators available, and we typically use strong-stability preserving variants of second and third-order Runge-Kutta schemes (RK2 and RK3, respectively) for GRMHD problems (Gottlieb et al. 2009).

3.3. Atmosphere Treatment

Because a number of operations in an Eulerian code lead to division by ρ or D , there must be a special treatment for vacuum regions. One common solution is to add an artificial low-density atmosphere in these regions. Though unphysical, one generally assumes that a sufficiently rarefied atmosphere will not significantly affect the evolution.

In practice, however, the atmosphere treatment can influence both the evolution (e.g., Poudel et al. (2020)) and its overall stability. AthenaK adopts a relatively simple flooring scheme. We fill our atmosphere with a static fluid with density ρ_{atm} and temperature T_{atm} . If $\rho < f_{\text{thr}} \rho_{\text{atm}}$ after reconstruction or the conserved-to-primitive inversion for some user-specified f_{thr} , ρ and T are reset to ρ_{atm} and T_{atm} , respectively, the velocity is zeroed, and P is recalculated. If $T < T_{\text{atm}}$, T is reset and P recalculated, but both ρ and Wv^i are left alone. A similar policy holds for the conserved variables. For given values of D and B^i , a floor $\tau_{\text{atm}}(D, B^i)$ assuming $T = T_{\text{atm}}$ can be calculated. If $\tau < \tau_{\text{atm}}$, τ is reset to $\tau_{\text{atm}}(D, B^i)$. If $D < f_{\text{thr}} \rho_{\text{atm}}$, we set $D = \rho_{\text{atm}}$, $S_i = 0$, and $\tau = \tau_{\text{atm}}(D_{\text{atm}}, B^i)$. In all cases, B^i is left alone to preserve the divergence-free condition. However, if $B^2/D > M_{\text{max}}$, we reset $D = B^2/M_{\text{max}}$.

Though this procedure generally allows for stable evolutions, it artificially injects mass and heat into the fluid and removes momentum from the system. To help address this, both the Valencia and HARM-like GRMHD solvers use a first-order flux correction (FOFC) (Lemaster & Stone 2009). After the flux calculation, the next Runge-Kutta step is estimated. If any cell in the new state requires a floor or the conserved-to-primitive inversion (see 3.4) fails, it is flagged. We then recalculate the fluxes for all flagged cells using a more dissipative scheme; namely, we reduce reconstruction to first order (donor-cell reconstruction) and recalculate the fluxes using LLF or HLLE. This scheme is guaranteed to be positivity-preserving for D (and τ in flat space). While this does not eliminate the need for a floor or even ensure that D cannot fall below the floor (e.g., rarefaction waves in strong explosions), it does prevent floors caused by spurious oscillations near discontinuities, such as stellar surfaces or shocks, and it also adds a small amount of dissipation where a state might become unphysical. We also stress that FOFC is only an estimate; we do not apply source terms, perform constrained transport, or update the matter fields prior to testing the solution.

One shortcoming of the proposed FOFC method is that it only identifies unphysical states by failures during the primitive variable recovery. However, unphysical behavior, such as carbuncles or spurious oscillations, may develop over several time steps before the conserved-to-primitive inversion fails. Attempting to fix these errors after the fact using FOFC may prevent the inversion failure, but it does not correct the unphysical state itself.

In an attempt to address this problem, consider the following: scalar conservation laws obey a maximum principle (Kruřkov 1970). That is, for

$$\partial_t u + \partial_i f^i(u) = 0, \quad (10)$$

it follows that for $u(x, t)$,

$$\min_x u(x, 0) \leq u(x, t) \leq \max_x u(x, 0). \quad (11)$$

When this equation is discretized, such as in a finite-volume scheme, a similar notion holds, known as the local discrete maximum principle (DMP). The DMP does not strictly hold for a system of conservation laws like the GRMHD equations, but we can use it as a starting point for a scheme which limits excessive growth. Let U_i^n represent a state at time $t = n\Delta t$ averaged over the cell centered on position x_i . We also define \mathcal{V}_i as the set containing the cell at x_i and all its immediate neighbors, including corner cells. For $M \geq 1$, we require that

$$\frac{1}{M} \min_{j \in \mathcal{V}_i} U_j^n \leq U_i^{n+1} \leq M \max_{j \in \mathcal{V}_i} U_j^n. \quad (12)$$

We may consider this a sort of *relaxed* DMP. The GRMHD equations are not required to obey the relaxed DMP, either, but for an appropriately chosen $M \geq 1$, applying the FOFC where it is violated will add additional dissipation to help limit spurious oscillations or numerical instabilities. In the tests which follow, we choose M somewhat arbitrarily (typically $M = 1.1$ or $M = 1.2$) to damp large oscillations while still allowing some growth. Detailed analysis or numerical experiments may reveal an optimal value for a given problem or set of equations, but this is beyond the scope of this work. Our own implementation also only enforces the DMP on D and τ , as enforcing the maximum principle on S_i is both unphysical and adds excessive dissipation. Furthermore, we perform this step *before* the τ source terms are added during each substep of the time integration in order to avoid mistaking gravitational effects for physically spurious solutions. We refer to this method throughout the paper as FOFC+DMP. Note that this approach is not novel; the FOFC+DMP method we propose here may be considered a simplified version of a multi-dimensional optimal-order detection (MOOD) scheme, which selects the highest-order method satisfying physical constraints and an appropriate maximum principle (Clain et al. 2011; Zanotti et al. 2015).

3.4. Primitive Variable Recovery

A well-known difficulty with GRMHD concerns the conserved-to-primitive inversion problem. Though Eq. 6 provides a simple closed-form expression for the conserved variables in terms of the primitive variables, the inverse operation is transcendental for most equations of state (EOSs). Our approach to the problem is based on the algorithm presented in Kastaun et al. (2021). Though a reference library, `RePrimAnd`, exists for this problem (Kastaun 2021), we have implemented our own library, `PrimitiveSolver`², for use in `GR-Athena++` and `AthenaK` (Cook et al. 2023). The primary reason for this decision is that `RePrimAnd` extensively uses polymorphism and virtual functions, which are more challenging to use inside GPU kernels.

`PrimitiveSolver` uses a templated policy-based design which mimics many of the traditional features of polymorphism. A base class `EOS` depends on two template parameters, `EOSPolicy` and `ErrorPolicy`, which provide the particular EOS implementation and error response (including the atmosphere treatment). Unlike traditional polymorphism, however, `EOS` inherits directly from both `EOSPolicy` and `ErrorPolicy`, rather

² see <https://github.com/jfields7/primitive-solver>

Table 1. Initial conditions for the Balsara shock tube tests, consisting of a Riemann problem with discontinuity located at $x = 0.5$ with left (L) and right (R) states.

Test	State	Γ	ρ	P	v^x	v^y	v^z	B^x	B^y	B^z
1	L	2	1	1	0	0	0	0.5	1	0
	R		0.125	0.1	0	0	0	0.5	-1	0
2	L	5/3	1	30	0	0	0	5	6	6
	R		1	1	0	0	0	5	0.7	0.7
3	L	5/3	1	10^3	0	0	0	10	7	7
	R		1	0.1	0	0	0	10	0.7	0.7
4	L	5/3	1	0.1	0.999	0	0	10	7	7
	R		1	0.1	-0.999	0	0	10	-7	-7
5	L	5/3	1.08	0.95	0.4	0.3	0.2	2	0.3	0.3
	R		1	1	-0.45	-0.2	0.2	2	-0.7	0.5

than EOS holding pointers to abstract policy classes whose concrete derived classes implement these features. Therefore, customizable EOS or error calls can be made on the GPU because the appropriate template functions are resolved at compile time rather than via a virtual method table at runtime.

The version of `PrimitiveSolver` included in `AthenaK` supports ideal gases and piecewise polytropic hybrid EOSs, and microphysical tabulated EOSs are currently being tested. For more information, including algorithmic differences from `RePrimAnd`, we refer the reader to the appendix of [Cook et al. \(2023\)](#).

4. TESTS

In this section, we describe a number of tests to validate `AthenaK`.

4.1. Magnetized Shock Tubes

As a first test, we consider a set of magnetized shock tubes in one dimension, following the standard setups in flat space presented by [Balsara \(2001\)](#). We summarize the initial conditions in [Table 1](#). Each shock tube consists of a Riemann problem with constant left and right states separated by a discontinuity at $x = 0.5$ on a domain of $[0, 1]$.

Our computational domain contains 1600 cells. We use the LLF Riemann solver with PPM4 reconstruction. Because the fluid solver remains stable during this test and never approaches atmosphere, we do not enable the FOFC scheme. We evolve these systems to $t = 0.5$ and compare them to their corresponding exact solutions ([Giacomazzo & Rezzolla 2006](#)) in [Figure 1](#). For brevity, we only show the x -component of velocity and the y -component of the magnetic field. The results are in good agreement with the exact solution.

We also perform additional tests with 100, 200, 400, 800, and 3200 cells in order to estimate convergence

as measured by the L^2 norm of the error in density. We show these results in [Figure 2](#). Some of the lower-resolution solutions do not appear to be in a completely convergent regime, most notably for Balsara Tests #3 and #5. However, we do achieve approximate first-order convergence for all tests, as expected for solutions dominated by shocks.

4.2. Magnetized Cylindrical Blast Wave

Our second test considers a magnetized cylindrical blast wave in flat spacetime following [Komissarov \(1999\)](#). The domain is filled with a static low-density, low-pressure fluid of ρ_{amb} and P_{amb} . Inside a specified inner radius, r_{in} , we set ρ_{in} and P_{amb} . From r_{in} out to an outer radius r_{out} , ρ and P decay exponentially. The magnetic field is set to $B^i = (B_x, 0, 0)$.

For this test, we set $\rho_{\text{amb}} = 10^{-4}$, $P_{\text{amb}} = 3 \times 10^{-5}$, $\rho_{\text{in}} = 10^{-2}$, $P_{\text{in}} = 1$, $r_{\text{in}} = 0.8$, and $r_{\text{out}} = 1.0$. We consider three values for the magnetic field: $B_x = 0.01$, $B_x = 0.1$, and $B_x = 1.0$. The EOS is an ideal gas with $\Gamma = 4/3$. As noted in [Beckwith & Stone \(2011\)](#), this test is particularly difficult for large B_x because the combination of relatively high Lorentz factors and high magnetizations heavily often causes the conserved-to-primitive inversion to return poor-quality solutions (if it finds them at all). Common solutions to this issue involve altering the test (e.g., increasing the ambient pressure as in [Leismann et al. \(2005\)](#); [Del Zanna et al. \(2007\)](#); [Beckwith & Stone \(2011\)](#); [Deppe et al. \(2023\)](#)) or employing schemes which violate energy conservation ([Komissarov 1999](#); [Mignone & Bodo 2006](#); [Phillips & Komissarov 2024](#); [Komissarov & Phillips 2024](#)). Consequently, the original setup as in [Komissarov \(1999\)](#) tests both the robustness of our primitive recovery routine and the ability of the FOFC and FOFC+DMP schemes to add enough dissipation to limit unphysical behavior.

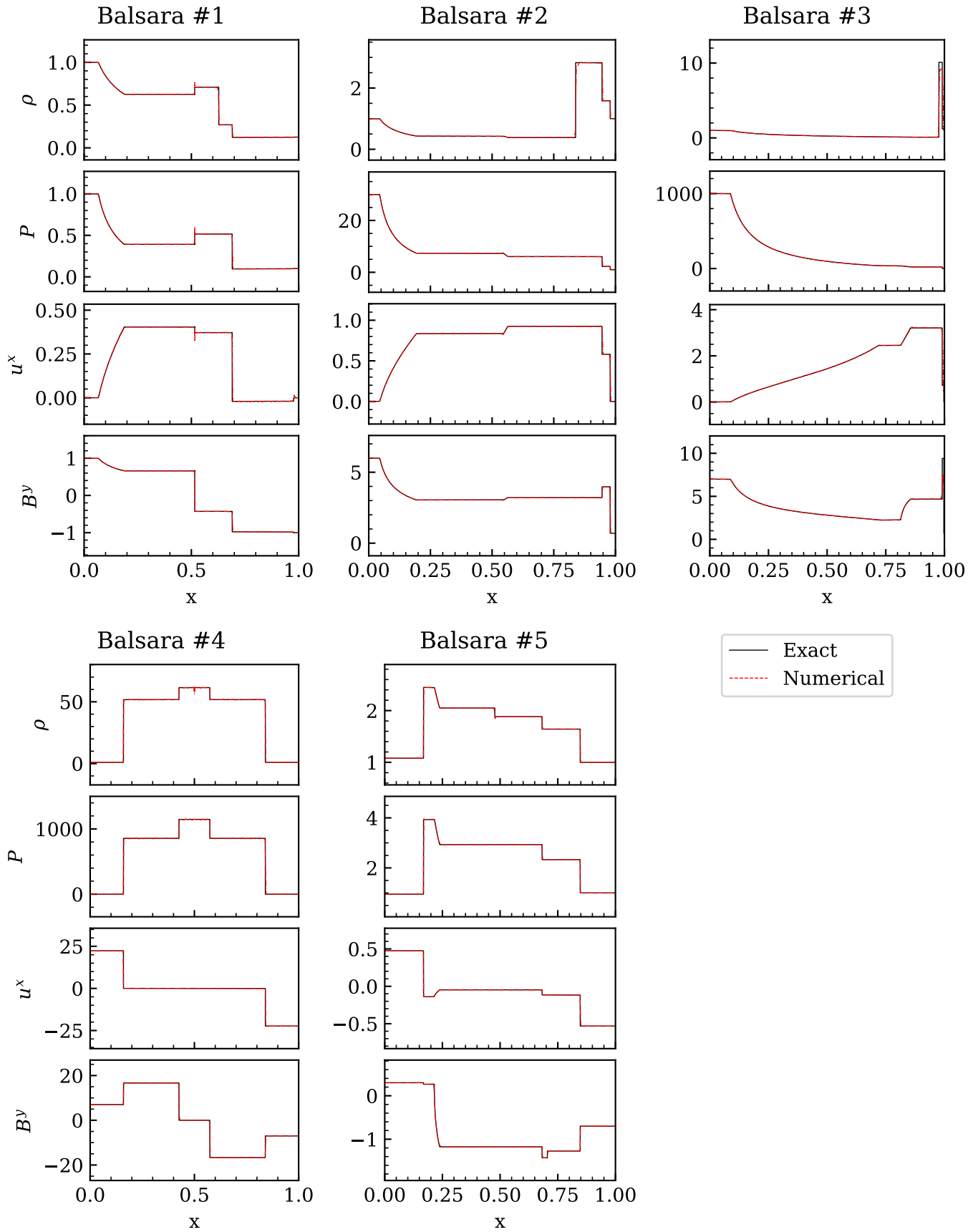


Figure 1. The rest-mass density ρ , pressure P , x -velocity $u^x = Wv^x$, and y -component of the magnetic field B^y for the shock tube tests at $t = 0.5$.

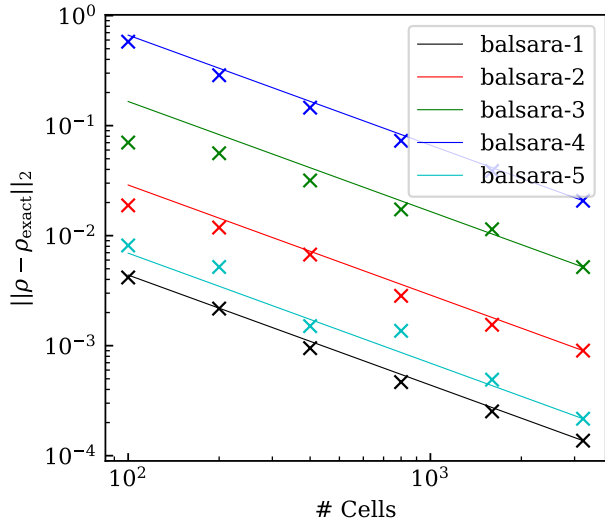


Figure 2. Shock tube convergence as measured by the L^2 error between the numerical and exact solutions for ρ at $t = 0.5$. Markers indicate numerical solutions, and solid lines measure first-order convergence.

The computational domain is a 2D Cartesian grid spanning $[-6.0, 6.0]$ with 200 cells in each direction. We employ HLLE as our Riemann solver, use WENOZ for reconstruction, and evolve in time with RK3 using $CFL = 0.1$. We set the floor to $\rho_{\text{atm}} = 10^{-10}$ and $T_{\text{atm}} = 10^{-8}$ with $f_{\text{thr}} = 1.0$. For the FOFC+DMP run, we set $M = 1.1$.

We show the results for the $B_x = 0.01$ case in Figure 3, the $B_x = 0.1$ case in Figure 4, and $B_x = 1.0$ in Figure 5. Both the FOFC and FOFC+DMP schemes are in good agreement for the weakly and moderately magnetized cases. The strongly magnetized case exhibits significant noise for both solutions, with FOFC+DMP offering somewhat better behavior near the center. Nevertheless, the overall solution agrees with Komissarov (1999), and our results are consistent with what was found for the same test using the HARM-like solver (Stone et al. 2024).

We also ran tests of the strongly magnetized case without FOFC (not pictured) to validate our claims of added stability; a test with PLM did not resolve the bar feature in Figure 5 as clearly, and the surrounding blast wave showed strong instabilities which rendered the solution useless. A test with WENOZ quickly disintegrated due to primitive inversion failures resetting the solution to atmosphere. With adjustments to the atmosphere and the error policy, it is possible that we could have improved stability in the non-FOFC solution. However, these are only stopgap measures which do not address the real problem: the solution is becoming unphysical.

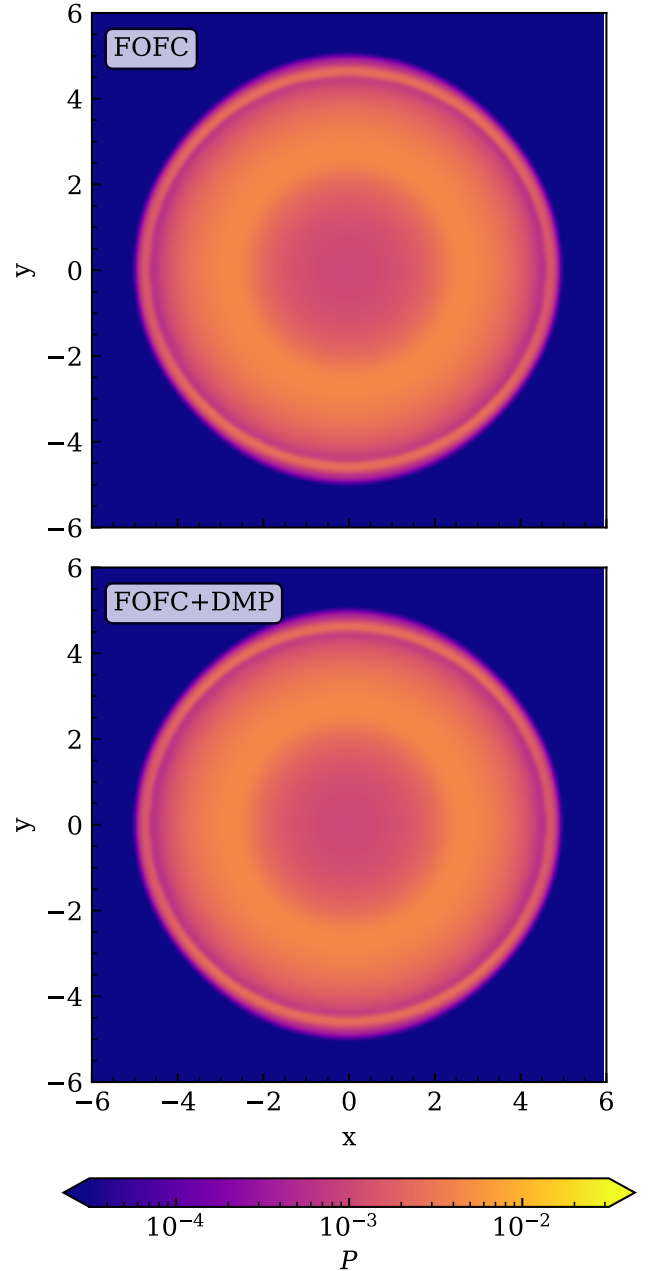


Figure 3. The pressure of a weakly magnetized blast wave ($B_x = 0.01$) at $t = 4$ for the FOFC (top) and FOFC+DMP (bottom) methods.

The FOFC and FOFC+DMP methods represent simple ways to add dissipation where the worst instabilities would develop while using a more accurate scheme in better-behaved regions.

4.3. Magnetic Loop Advection

This next test considers a two-dimensional magnetic loop which is advected at constant velocity (DeVore 1991). As in Gardiner & Stone (2005); Beckwith &

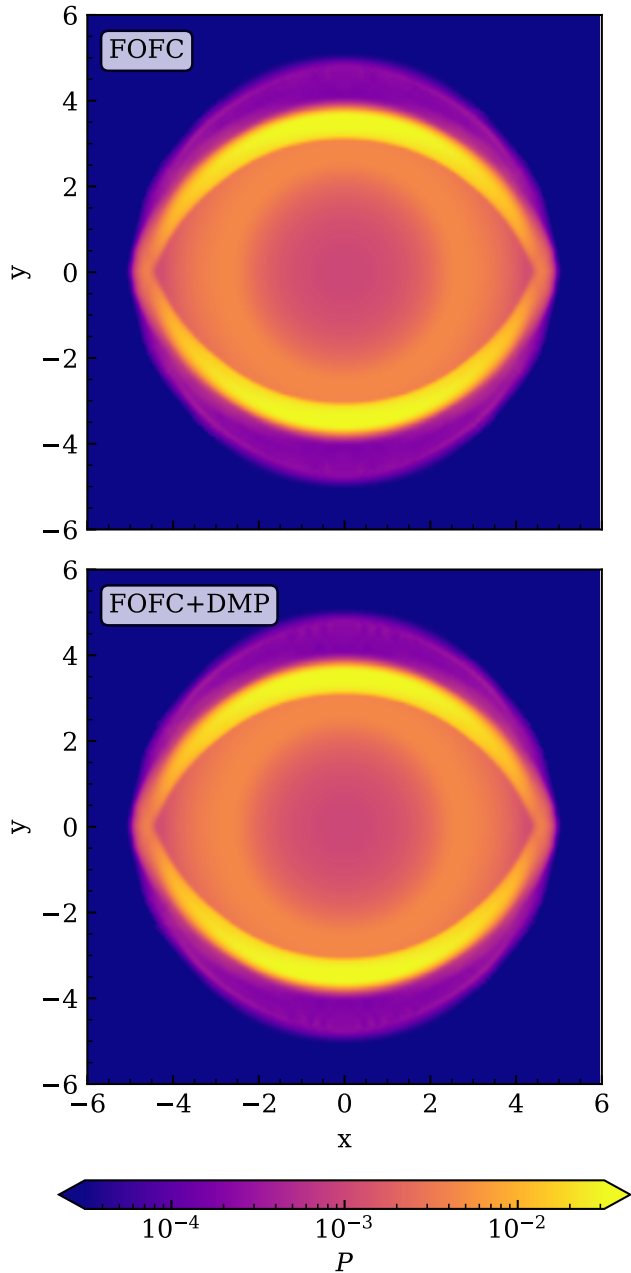


Figure 4. The same as Figure 3, but for a moderately magnetized blast wave ($B_x = 0.1$)

Stone (2011), the magnetic field components B^x and B^y are calculated from a vector potential,

$$A_z = \begin{cases} A_0(R - r) & r \leq R \\ 0 & r > R, \end{cases} \quad (13)$$

where $r = \sqrt{x^2 + y^2}$. Our setup most closely resembles Deppe et al. (2023), where we fix $A_0 = 10^{-3}$, $R = 0.3$, $\rho = 1$, $P = 3$, and $\mathbf{v} = \{1/1.2, 1/2.4, 0\}$ on a periodic domain covering $[-0.5, 0.5] \times [-0.5, 0.5]$ with 240^2 cells.

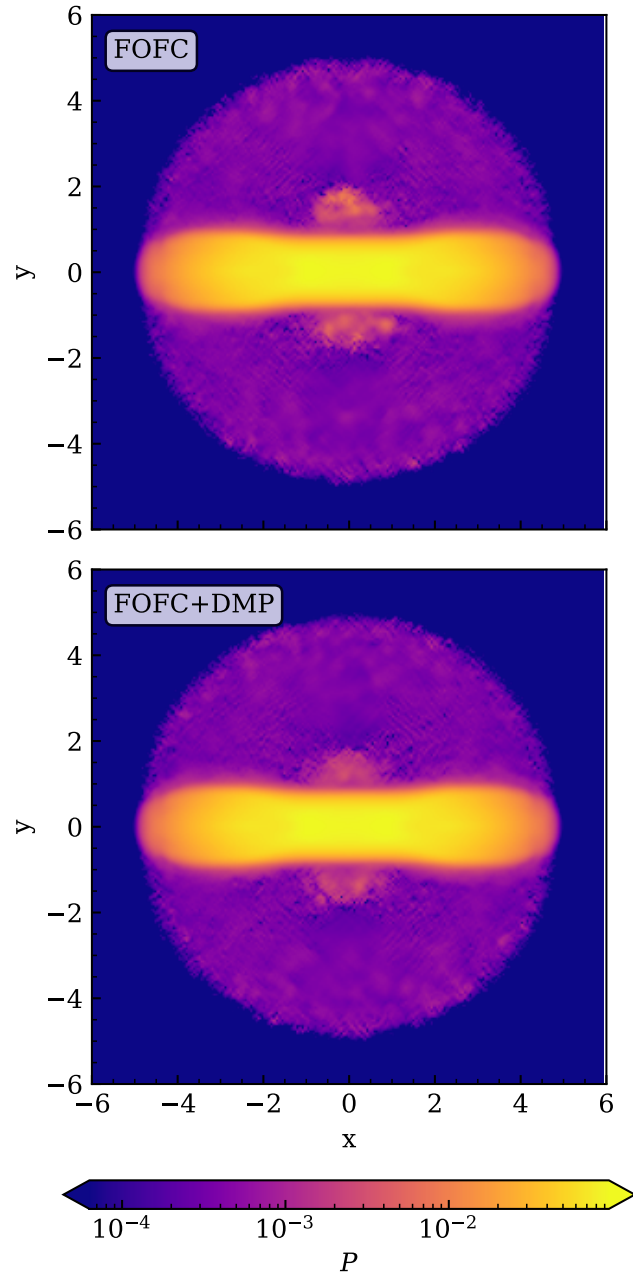


Figure 5. The same as Figure 3, but for a strongly magnetized blast wave ($B_x = 1.0$)

For this test, we use RK3, HLLC+FOFC, and WENO5 and evolve a single period ($t = 2.4$) with a CFL of 0.25.

This test probes the correctness and the diffusiveness of the constrained-transport scheme. As shown in Figure 6, AthenaK advects the loop at the correct speed. Some numerical diffusion is apparent, but the shape is correct with no obvious artifacts. Maximum relative errors in the divergence-free condition are around 7×10^{-14} and primarily concentrated around the edge of the loop. After a single period, the maximum error has amplified

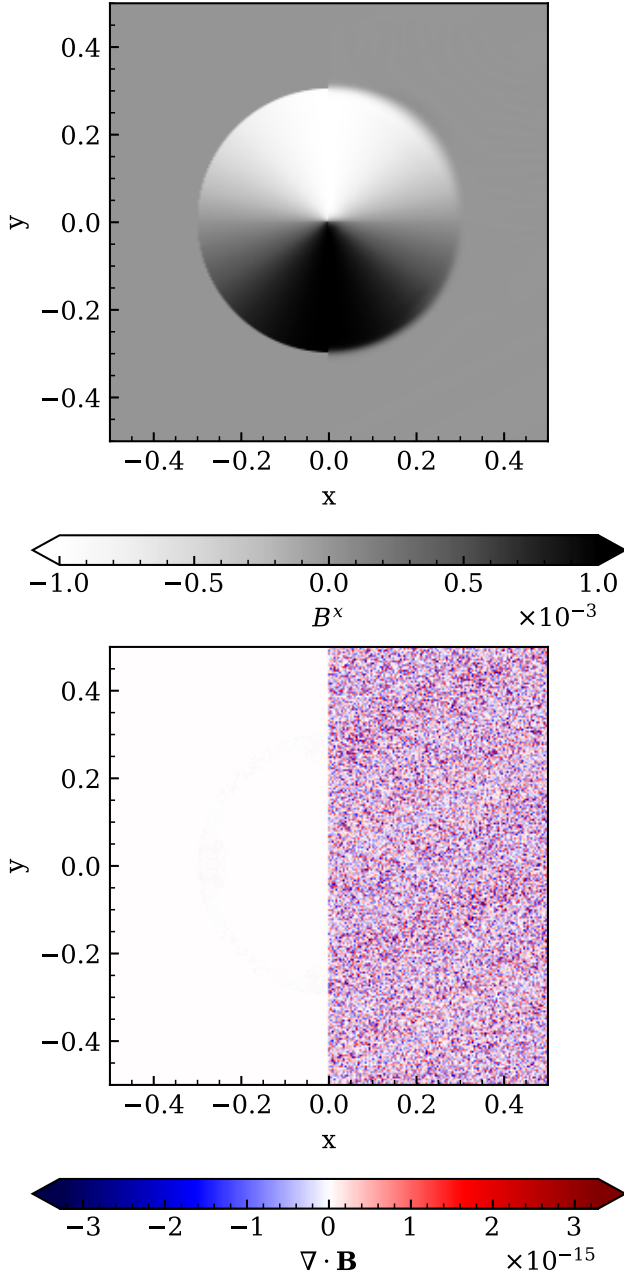


Figure 6. (Top) The B^x component of the magnetic field during the loop advection test. (Bottom) The violation of the divergence-free constraint relative to the maximum magnetic field strength. In both plots, the left half shows the initial data, and the right half shows the evolved data after a single period ($t = 2.4$).

to approximately 3×10^{-12} , which is consistent with growth from floating-point errors.

4.4. Oscillating Neutron Star in the Cowling Approximation

Our first test in curved spacetime considers linear perturbations to a Tolman-Oppenheimer-Volkoff (TOV)

star. Our test setup is designed to replicate the isolated neutron star tests in Radice et al. (2014a) as closely as possible. For these tests, we adopt HLLE as our Riemann solver with PPM4 reconstruction.

The computational domain spans $[0 M_\odot, 102.4 M_\odot]$ in all dimensions with vacuum boundary conditions and a reflection symmetry along the x , y , and z axes. The base refinement level has 128 cells in each direction, and we use static mesh refinement (SMR) to refine all mesh blocks inside $51.2 M_\odot$ and then again at $25.6 M_\odot$ to give the innermost refinement region a resolution of $0.2 M_\odot$. We set the Courant-Friedrich-Lewy (CFL) factor to $\text{CFL} = 0.4$.

The TOV solver uses the polytrope $P = K\rho^\Gamma$ with $K = 100$, $\Gamma = 2$, and central density $\rho_c = 1.28 \times 10^{-3} M_\odot^{-2}$, which results in a single star with mass $M = 1.4 M_\odot$ and radius (in Schwarzschild coordinates) of $R \approx 9.59 M_\odot$. We also perform our test in the Cowling approximation, i.e., with spacetime evolution disabled, and we do not add a magnetic field. To match the setup in Radice et al. (2014a), we set $\rho_{\text{atm}} = 10^{-10} M_\odot^{-2}$ and $f_{\text{thr}} = 1.01$. Because we evolve the system with an ideal gas, we also add a temperature floor of $T = 10^{-8} M_\odot$.

To induce a small perturbation in the velocity, we use the radial velocity eigenfunction of Novak (2001); Noble & Choptuik (2008),

$$v_r(r) = \frac{U}{2}(3x - x^3), \quad (14)$$

with $x \equiv r/R$ and U indicating the amplitude of the profile at stellar surface. For our tests, we use $U = -0.024$, representing an inward perturbation.

We plot the central density oscillations in time and frequency space in Figure 7. All three methods also show excellent agreement in oscillations of the central density; the power spectrum of these oscillations also show that all three methods differ from the peak frequency and its first harmonic as predicted by perturbation theory by 47 Hz and 20 Hz, respectively (Stergioulas et al. 2004). The frequency resolution is ~ 20 Hz, suggesting that the error is small even at this relatively coarse resolution. Nevertheless, the low resolution does cause a slow downward drift in the central density. The similarity of the results indicates that the FOFC and FOFC+DMP methods have minimal effects on stability, accuracy, and damping time. This is expected, as these methods should only trigger to prevent primitive inversion failures or unnecessary flooring.

4.5. Free Evolution of an Oscillating Neutron Star

To test the spacetime evolution, we consider the same test as 4.4 but with all symmetry removed and the Z4c

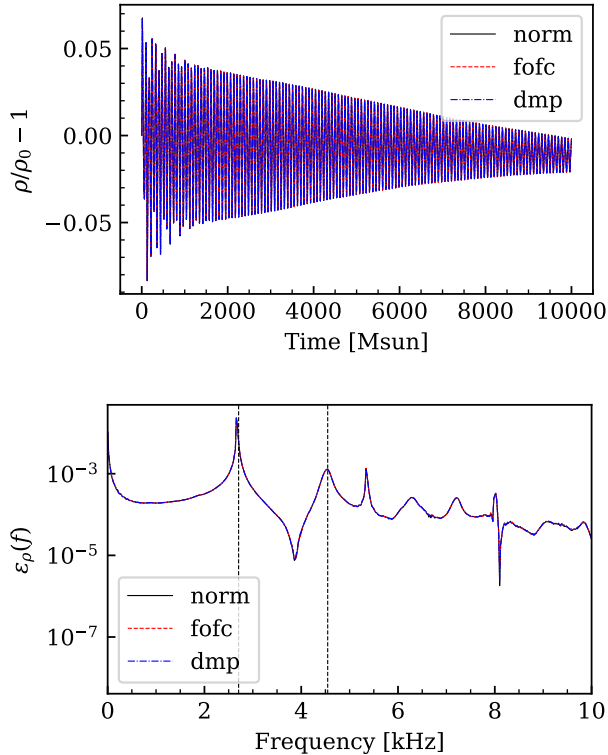


Figure 7. Oscillations of the central density of the TOV star as a function of time (top) and the power spectrum of central density oscillations (bottom). The ‘norm’, ‘fofc’ and ‘dmp’ labels refer to runs without FOFC, with FOFC, and with FOFC+DMP, respectively. To reduce spectral leakage, the oscillations were filtered with a Tukey window of $\alpha = 0.203$ prior to computing the Fourier transform. The black vertical lines mark the fundamental frequency and its first harmonic as predicted by perturbation theory.

solver enabled. We also do not apply an explicit perturbation and instead rely on discretization errors to excite oscillations. To improve gauge stability, we switch to isotropic coordinates, which slightly reduces the coordinate radius to $R \approx 8.13 M_\odot$. We extend the boundary out to $\pm 204.8 M_\odot$ in all directions and add four refinement levels, each successively halving the domain, such that the finest level spans $\pm 12.8 M_\odot$ in each direction. We perform tests with 192^3 and 384^3 cells on the base grid, which corresponds to resolutions of $\Delta x \approx 0.133 M_\odot$ ($\Delta x \approx 197$ m) and $\Delta x \approx 0.0667 M_\odot$ ($\Delta x \approx 98$ m) on the finest refinement level. We additionally change the atmosphere to $\rho_{\text{atm}} = 1.28 \times 10^{-13}$, $T_{\text{atm}} = 1.28 \times 10^{-11}$, and $f_{\text{thr}} = 0.1$ (i.e., the density is allowed to drop below the atmosphere). To improve accuracy near the center of the star, we switch the reconstruction algorithm to WENOZ. Like the Cowling case, we perform tests with no FOFC, with FOFC, and with FOFC+DMP.

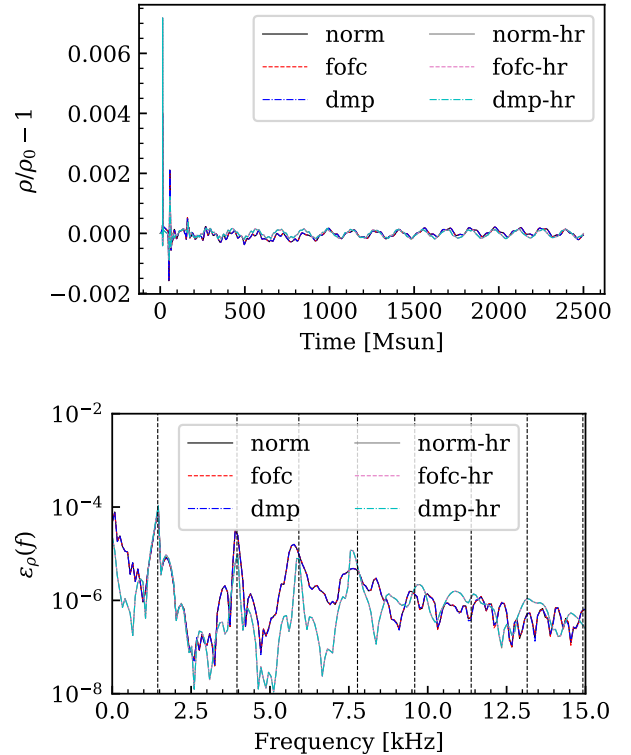


Figure 8. The same as Figure 7, but for a TOV star with the Z4c solver enabled. The ‘norm’, ‘fofc’, and ‘dmp’ labels refer to runs without FOFC, with FOFC, and with FOFC+DMP, respectively. Labels without the ‘-hr’ suffix refer to the 192^3 runs, and those with the 384^3 solutions.

Figure 8 shows the central density oscillations and their power spectrum. Following an initial spike as the TOV solution settles onto the computational grid, the oscillations remain quite small without strong damping or indications of secular drift. As in the Cowling approximation, all three methods demonstrate good agreement with the oscillation frequencies predicted by perturbation theory (Yoshida & Eriguchi 2001). The 192^3 solution has errors of 19 Hz, 56 Hz, and 149 Hz compared to the predicted values for the fundamental and the first and second harmonics, respectively. The errors of both the fundamental and the first harmonic are less than the frequency resolution (~ 81 Hz). The third harmonic also seems to be present and has a fairly low error around 141 Hz, but the width and relatively low amplitude of this peak suggest it may not be reliable. The 384^3 solution has errors of 19 Hz, 25 Hz, 68 Hz, and 222 Hz for the fundamental frequency and the first, second, and third harmonics. The third harmonic is the first with an error exceeding the finite frequency resolution. The fourth harmonic has an error of 157 Hz, though this peak, as well as those which follow, may not be reliable.

4.6. Magnetized Accretion Disk

In this test, we simulate the development of the magnetorotational instability (MRI) inside an accretion disk in a fixed spacetime. We use initial conditions which are similar to the Event Horizon Telescope (EHT) code comparison test (Porth et al. 2019), which consists of a Fishbone-Moncrief torus (Fishbone & Moncrief 1976) surrounding a Kerr black hole of mass M with dimensionless spin $a = 0.9375$. The torus begins at an inner radius $r_{\text{in}} = 6M$ and extends to an outer radius $r_{\text{out}} = 12M$ with a magnetic field defined by the vector potential

$$A_\phi = A_0 \max(\rho/\rho_{\text{max}} - 0.2, 0), \quad (15)$$

where A_0 is set so that $\beta = 2P/b^2 = 100$. We assume an ideal gas with $\Gamma = 4/3$, and we add random perturbations to the pressure which are uniformly distributed in the range $[-0.02P, 0.02P]$ to help excite the MRI. Outside the torus, the background density and pressure are set to $\rho = 1.0 \times 10^{-5} r^{-3/2}$ and $P = 3.33 \times 10^{-8} r^{-5/2}$ in code units, and we choose flooring parameters $\rho_{\text{atm}} = 10^{-10}$, $P_{\text{atm}} = 3.33 \times 10^{-13}$ (for the HARM-like formulation), and $T_{\text{atm}} = 3.33 \times 10^{-13}$ (for the Valencia formulation) in code units.

We evolve the torus with both the new Valencia GRMHD solver and the existing HARM-like solver with RK2, HLLE+FOFC, and PPM4 to $t = 10000M$ on a domain spanning $\pm 64M$ in each direction with four levels of refinement, each successively halving the size of the grid. Each system is run at three resolutions; the base grid has 64^3 , 96^3 , and 128^3 cells, and the mesh blocks have a width of 16, 24, and 32 cells, respectively. This leads to resolutions of $\Delta x_{64} = 0.125M$, $\Delta x_{96} = 0.0833M$, and $\Delta x_{128} = 0.0625M$ on the finest refinement level. We excise the region $r \leq M$ and fill it with atmosphere to improve stability inside the horizon. The magnetic field is not modified during excision.

The purpose of this test is two-fold: first, it validates the Valencia GRMHD solver in curved space by showing it is in agreement with the HARM-like solver. Because the two solvers are physically equivalent, we expect that they should converge to the same results.

Secondly, it allows us to compare the strengths and weaknesses of these different formulations. As shown in Sec. 2, the HARM-like and Valencia formulations treat the energy evolution differently, so we expect that they should display different numerical properties. In particular, by evolving T_0^0 instead of E , the HARM-like formulation should exactly conserve the fluid energy in any stationary spacetime. This may also lead to a more stable evolution in the strong-field regime, where E or τ in the Valencia formulation can develop large source terms

which may cause issues with round-off error or preserving positivity. However, it is not immediately clear how important these effects are in a full nonlinear evolution.

Though some of the codes used in the EHT code comparison test, including ECHO (Del Zanna et al. 2007), BHAC (Porth et al. 2017), and IllinoisGRMHD (Etienne et al. 2015), use the Valencia formulation and achieve similar results to codes using a HARM-like formulation, there are differences in grid setups and numerical methods which make a one-to-one comparison difficult. Porth et al. (2017) provide a more consistent comparison and find good agreement, but their analysis is limited to the mass accretion rate and magnetic flux in a 2D axisymmetric problem.

To compare the consistency in evolution, we use the following radial fluxes as diagnostics:

$$\dot{M} = \int_0^{2\pi} \int_0^\pi \rho u^r \sqrt{-g} d\theta d\phi, \quad (16a)$$

$$\dot{E} = \int_0^{2\pi} \int_0^\pi -T_t^r \sqrt{-g} d\theta d\phi, \quad (16b)$$

$$\dot{L} = \int_0^{2\pi} \int_0^\pi T_\phi^r \sqrt{-g} d\theta d\phi, \quad (16c)$$

$$\Phi_B = \frac{1}{2} \int_0^{2\pi} \int_0^\pi |b^r u^0 - b^0 u^r| \sqrt{-g} d\theta d\phi, \quad (16d)$$

where we integrate over a sphere with a fixed Kerr-Schild radius r . In practice this means the integration surface is oblate in the usual Cartesian coordinates, and we interpolate our primitive variables to an appropriate geodesic grid first.

We show these diagnostic quantities in Figure 9 for each run. For comparison, the plots also contain a subset of the data from Porth et al. (2019) (hereafter referred to as the EHT data), namely Athena++, BHAC, Cosmos++ (Anninos et al. 2005; Fragile et al. 2012; Fragile et al. 2014), ECHO, HARM-Noble (usually called HARM3d) and iharm3D (Gammie et al. 2003; Noble et al. 2006, 2009), IllinoisGRMHD, and KORAL (Sadowski et al. 2013; Sadowski et al. 2014). Somewhat confusingly, we compare the 64^3 AthenaK runs to the 96^3 EHT data, the 96^3 runs to the 128^3 EHT data, and the 128^3 runs to the 192^3 EHT data. This is because the AthenaK grids do not have a direct correspondence with any setup in the EHT data; all AthenaK setups are Cartesian, while most of the EHT data setups are on logarithmic spherical grids. Nevertheless, we see good agreement between AthenaK and the other codes present at all resolutions, particularly for the angular momentum flux and the mass accretion rates.

To examine this more carefully, Figure 10 plots the averages of each of the diagnostic fluxes over the range

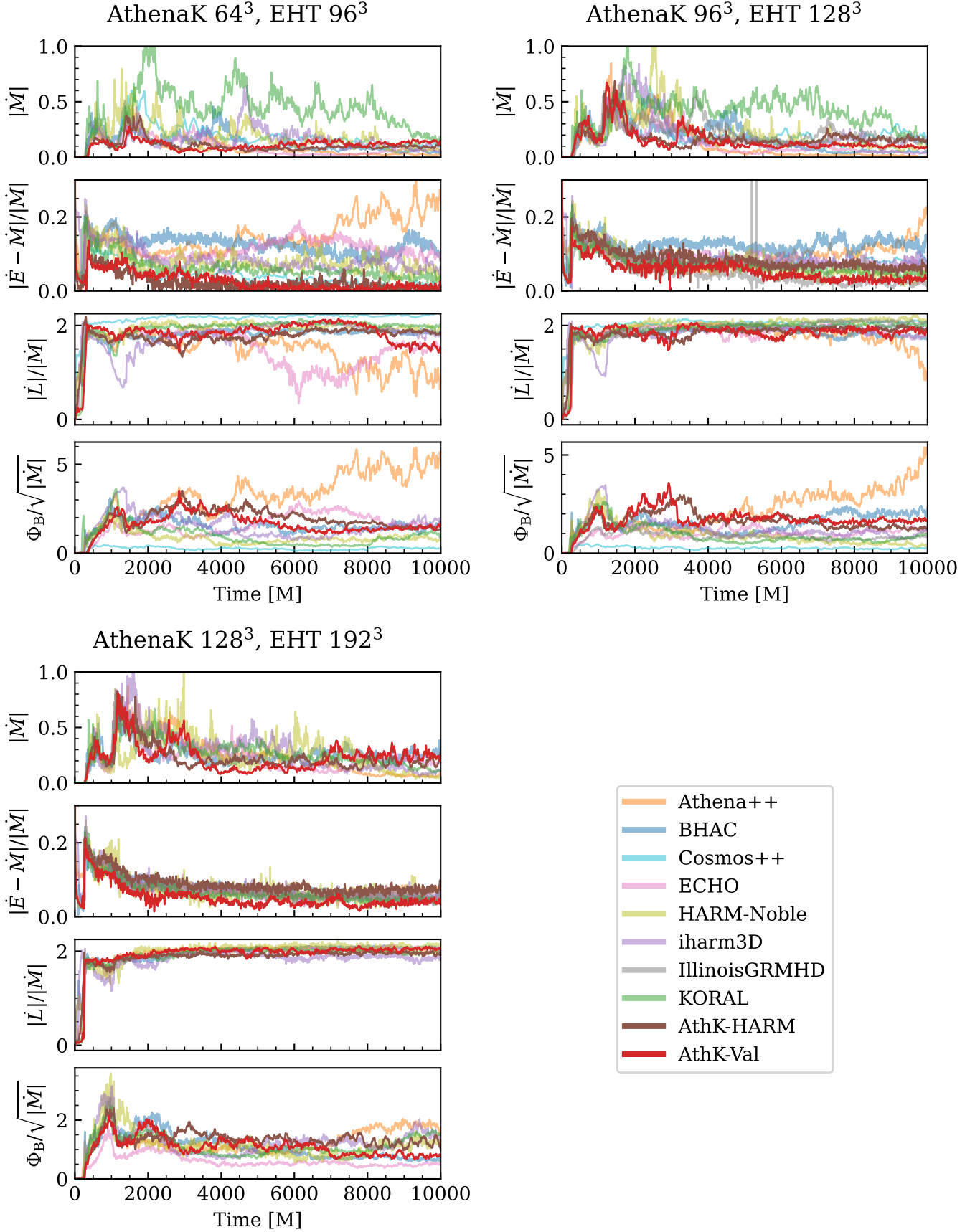


Figure 9. Diagnostic fluxes for the 64^3 , 96^3 , and 128^3 cases plotted against some of the 96^3 , 128^3 , and 192^3 EHT data (respectively). From top to bottom in each set of plots, we show the rates for mass accretion, normalized energy accretion, normalized angular momentum accretion, and normalized magnetic flux.

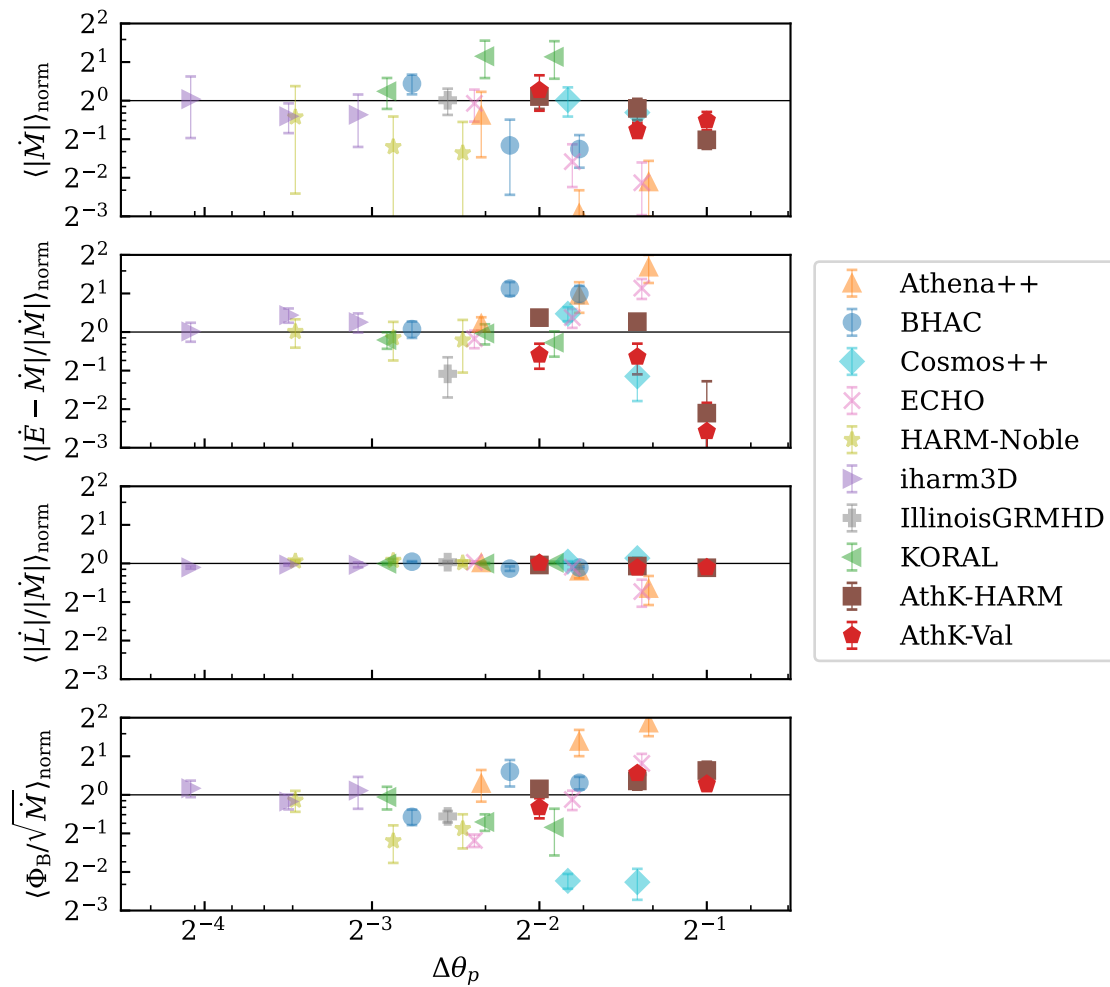


Figure 10. The average of the diagnostic fluxes over $t \in [5000M, 10000M]$ for each resolution, normalized by the average of all the codes considered. The error bars span a single standard deviation.

$t \in [5000M, 10000M]$, normalized to the total average for all the codes considered, as a function of resolution. Because most of the compared codes use spherical coordinates and differing grid setups, we follow Porth et al. (2019) and define a fiducial resolution, $\Delta\theta_p \equiv \sqrt{g_{\theta\theta}(12M, \pi/2)}\Delta\theta$, corresponding to the proper distance between polar grid cells at $r = 12M$ in the equatorial plane. We treat Δz as the equivalent quantity for the Cartesian runs. As seen in the time series plots, AthenaK is consistent with the expected results based on the EHT data, with the only true outlier being the energy accretion in the 64^3 test.

The 64^3 AthenaK runs do display a much lower value for $|\dot{E} - \dot{M}|/|\dot{M}|$ than other codes, but this appears to be an artifact of the resolution; both the 96^3 and 128^3 runs have energy accretion rates which are more consistent with other GRMHD codes. This is most likely because of the grid setup we have chosen. Though we have reasonable resolution near the horizon, with our 64^3 setup exceeding the resolution of the IllinoisGRMHD data, the resolution quickly falls off in the torus to $\Delta z = 0.5M$ at $(12M, 0, 0)$, which is lower than the fiducial resolution in any of the other codes.

When compared to each other, the HARM-like and Valencia solvers (denoted as “AthK-HARM” and “AthK-Val”, respectively) show no major differences except for the energy accretion rate, which is systematically lower for the Valencia solutions than in the equivalent HARM-like solutions. This may be related to the different treatment of the energy term between the two formulations. However, the 64^3 solution is clearly not in a convergent regime, so it is not immediately clear how robust this trend is. Furthermore, though they do not constitute the same one-to-one comparison, neither BHAC nor ECHO seem to be consistently lower than HARM-like codes at similar resolutions.

To better understand differences beyond the horizon, Figures 11–13 show contour plots of ρ averaged azimuthally over $\phi \in [0, 2\pi]$ and temporally over $t \in [5000M, 10000M]$ for each run. We additionally plot contour contours of the magnetization, $\sigma \equiv b^2/\rho$, and the inverse plasma-beta, $\beta^{-1} \equiv b^2/2P$, at $\sigma = 1$ and $\beta^{-1} = 1$. The σ contours loosely corresponds to the outermost boundary of the funnel (see, e.g. McKinney & Gammie (2004); Porth et al. (2019)), while β^{-1} marks the equipartition region and the transition from pressure being thermally dominated to magnetically dominated, and it often coincides with the boundary of the disk. The density inside the funnel region decreases with improved resolution for both solvers, with the HARM-like solver clearly favoring lower densities compared to the Valencia solver. We also see qualitative differences in

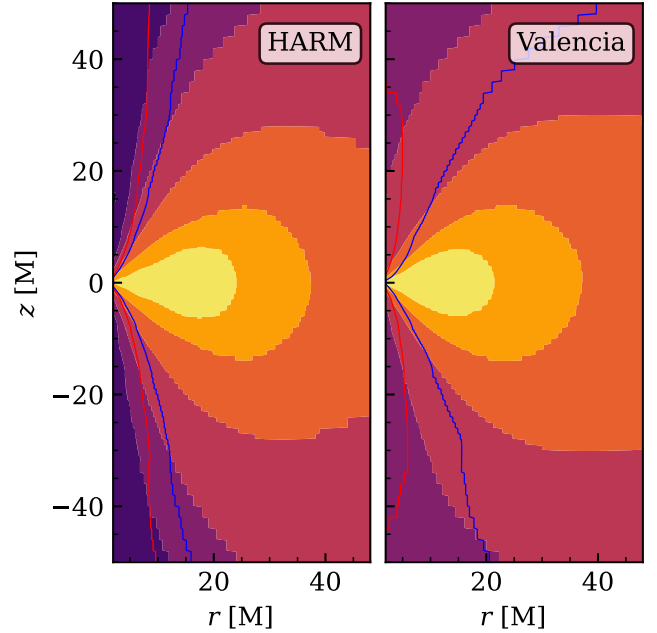


Figure 11. Contour plots for ρ azimuthally and temporally averaged over the range $\phi \in [0, 2\pi]$, $t \in [5000M, 10000M]$. The 64^3 HARM-like data is on the left, and the 64^3 Valencia data is on the right. There are six logarithmically spaced bins (i.e., seven contours) in the range $[10^{-7}, 1]$ in units of M^{-2} . The blue contour marks $\beta^{-1} = 1$, and the red contour indicates $\sigma = 1$.

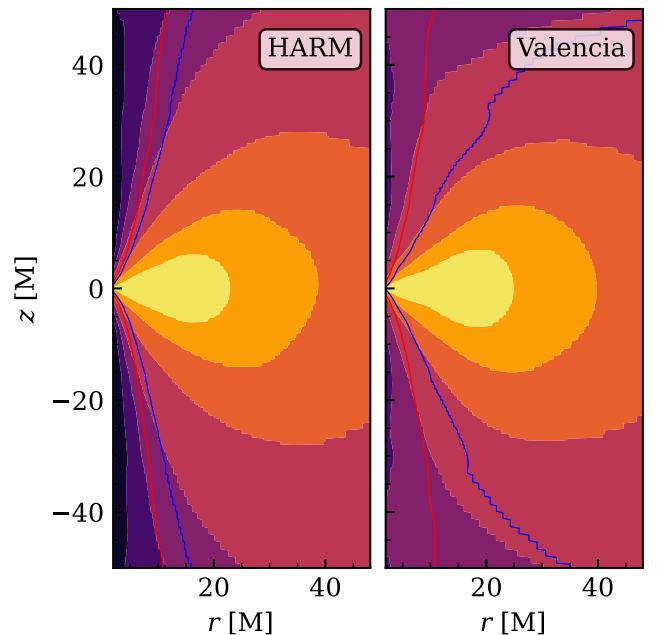


Figure 12. Same as Figure 11 but for the 96^3 data.

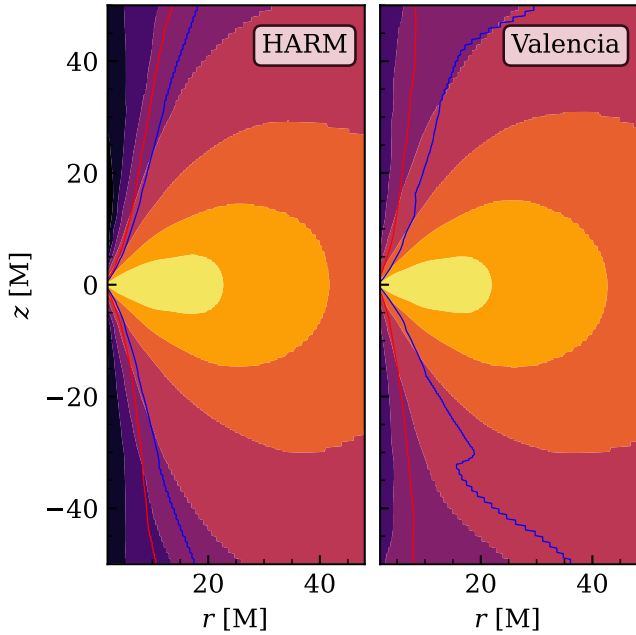


Figure 13. Same as Figure 11 but for the 128^3 data.

the funnel boundary; the size of the funnel is relatively stable in the HARM-like formulation but steadily increases with resolution, while the lowest contour in the Valencia formulation shows fairly significant changes in shape and size for each resolution. We see a similar trend for β^{-1} , where the HARM-like formulation favors a later transition from being thermally dominated to magnetically dominated and a much more stable shape.

The Fishbone-Moncrief torus is an equilibrium solution with uniform specific angular momentum $\ell = u_\phi u^t$, and the only way to accrete matter or bring it into the funnel is by material losing ℓ . Figure 14, which shows time-averaged, mass-weighted histograms of ℓ , suggests that the Valencia runs have more low- ℓ material than the HARM-like runs, which is in agreement with our expectations from Figures 11–13. The extra low- ℓ material cannot be attributed to significant differences in the amount of mass; the 64^3 and 128^3 Valencia runs have $\sim 4\%$ less mass than the HARM-like runs, and the 96^3 run contains $\sim 12\%$ more mass than the 96^3 HARM-like run. We also observe that the difference in the distribution of ℓ decreases with resolution, indicating that the two solvers appear to be converging toward similar results.

These differences may be linked to the lack of guaranteed energy conservation in the Valencia formulation. If the Valencia runs slowly lose energy, the angular momentum will also be affected, likely resulting in more low- ℓ material and a funnel containing more material. This would also explain the lower energy accretion rates seen relative to the HARM-like formulation. How-

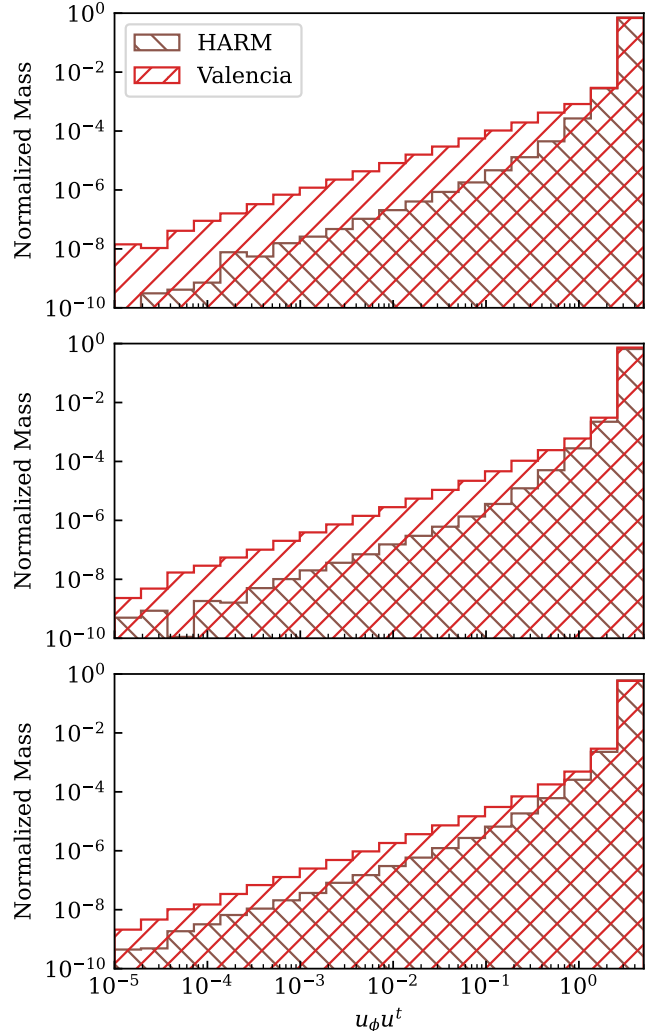


Figure 14. Mass-weighted histograms of the specific angular momentum $u_\phi u^t$ for the 64^3 (top), 96^3 (middle), and 128^3 (bottom) tests. Each distribution is temporally averaged over $t \in [5000M, 10000M]$. The distributions are then normalized against the initial mass at $t = 0$ and therefore do not add up to unity.

ever, though these tests are strongly suggestive that the GRMHD formulation causes these differences, they are hardly conclusive. Furthermore, the differences between either solver in *AthenaK* and other GRMHD codes at similar resolutions in the EHT data are generally larger than the differences caused by changing solvers. As resolution increases, both solvers also appear to converge toward similar results. We therefore conclude that one’s grid setup and choice of numerical scheme are more important than the specific GRMHD formulation.

4.7. Binary Neutron Star Merger

Our last accuracy test duplicates the BNS merger in [Cook et al. \(2023\)](#), which consists of an equal-mass bi-

nary with a total baryon mass $M_b = 3.25 M_\odot$ and a gravitational mass $M = 3.0297 M_\odot$ with an initial separation of 45 km and orbital frequency $f_0 \approx 294$ Hz. The data is constructed with the LORENE initial data code (Gourgoulhon et al. 2001; Gourgoulhon et al. 2016) assuming a polytropic EOS with $K \approx 123.6$ and $\Gamma = 2$.

The computational domain spans $[-1536 M_\odot, 1536 M_\odot]$ in every direction and uses seven layers of mesh refinement. We perform the test at three resolutions with 128^3 , 192^3 , and 256^3 cells on the base grid, which we respectively designate as LR, SR, and HR. This corresponds to resolutions of $\Delta x = \{0.1875 M_\odot, 0.125 M_\odot, 0.09375 M_\odot\}$, or $\Delta x \approx \{277 \text{ m}, 185 \text{ m}, 138 \text{ m}\}$, on the finest refinement level. We ensure that refinement structure remains the same by setting the mesh block size to 16, 24, and 32 cells per dimension for the LR, SR, and HR resolutions, respectively, resulting in 7960 total mesh blocks per run. To facilitate comparison with GR-Athena++, we use LLF and WENOZ, and we set $\rho_{\text{atm}} = 1.28 \times 10^{-21}$ and $T_{\text{atm}} = 1.58255 \times 10^{-19}$. Unlike GR-Athena++, AthenaK does not currently have an apparent horizon finder which can be used for excising the fluid inside a black hole. In order to ensure stability through collapse, we use an ad-hoc excision scheme by flooring all fluid variables inside the region $\alpha < 0.20$. Also differently from GR-Athena++, we enable FOFC and set $f_{\text{thr}} = 0.1$. Neither of these choices will strongly affect the waveform, but they improve mass conservation and the overall stability of our solution. However, we do not enable the DMP scheme, as this particular binary system should be well-behaved even with standard numerical methods. We also note that the GR-Athena++ run contains a poloidal magnetic field, which the AthenaK runs neglect. However, the magnetic field is not dynamically important for gravitational waves during the inspiral and early post-merger even for very large fields (Ioka & Taniguchi 2000; Giacomazzo et al. 2009; Palenzuela et al. 2015, 2022), so this difference should not affect our comparison.

As an additional comparison, we also perform an additional run with WhiskyTHC (Radice & Rezzolla 2012; Radice et al. 2014b,a, 2015) using a high-order conservative finite-difference method with MP5 reconstruction. WhiskyTHC is based on the EinsteinToolkit (Loffler et al. 2012; Brandt et al. 2024) and on the Carpet AMR driver, which implements Berger-Oliger patch-based refinement (Berger & Oliger 1984). Note that refluxing is not supported for the finite-differencing version of WhiskyTHC used here. We evolve the spacetime using the CTGamma code (Pollney et al. 2011; Reisswig et al. 2013), which solves the Z4c formulation of Einstein’s equa-

tions, like AthenaK. The WhiskyTHC simulations have 7 refinement levels. The finest one covers each star during inspiral and has a grid spacing $h = 0.125 M_\odot$. Time integration is performed with a 3rd-order strongly-stability preserving Runge-Kutta scheme. The CFL for the WhiskyTHC simulations is set to 0.125, to be able to use the positivity-preserving limiter in WhiskyTHC (Radice et al. 2014a).

We show the gravitational waveform extracted at $R = 500 M_\odot$ (except for the WhiskyTHC run, which was extracted at $R = 400 M_\odot$) in the top half of Figure 15 as a function of the retarded time, $t - r_*$, where $r_* = r + 2M \log(r/2M - 1)$ and $r(R) = (1 + M/2R)^2 R$. Our LR solution corresponds to the 128^3 solution for GR-Athena++ reported in Cook et al. (2023). We find excellent agreement between these two solutions through merger, and agreement still remains reasonable through the first several milliseconds of the post-merger phase. The difference in merger time is $\Delta t \approx 0.05$ ms, with AthenaK merging slightly earlier. The SR solution roughly corresponds to the WhiskyTHC results, and the two are in good agreement despite using different numerical methods; the difference in merger time between the two is $\Delta t \approx 0.01$ ms and sits approximately halfway between the LR run and GR-Athena++.

We do not see good agreement in collapse time; AthenaK’s LR solution collapses ~ 9 ms after merger, while the GR-Athena++ run does not collapse in the plotted duration. Similarly, WhiskyTHC predicts collapse around ~ 13 ms after merger, but the SR solution does not collapse during this time. There is also no consistency in the AthenaK runs in this region, with the HR solution collapsing after the LR run but before the SR case. However, collapse time is notoriously sensitive to perturbations, and even very similar numerical methods predict different collapse times (e.g., Espino et al. (2023)).

We use the SR and HR resolution runs to establish convergence of the waveform phase. To eliminate phase offsets caused by non-converging noise prior to the arrival of the so-called “junk” radiation at the extraction radius, we align the waveforms using the procedure in Boyle et al. (2008) between $t - r_* = 0$ and the merger time of the LR waveform. We show the results in the bottom plot in Figure 15. Throughout the inspiral and merger, we maintain approximate second-order convergence as expected by our numerical methods. The results do not show clean convergence in the post-merger phase even before collapse. However, we note that most NR codes struggle to maintain convergence in the post-merger phase, especially with second-order schemes (Bernuzzi et al. 2012b; Radice et al. 2015;

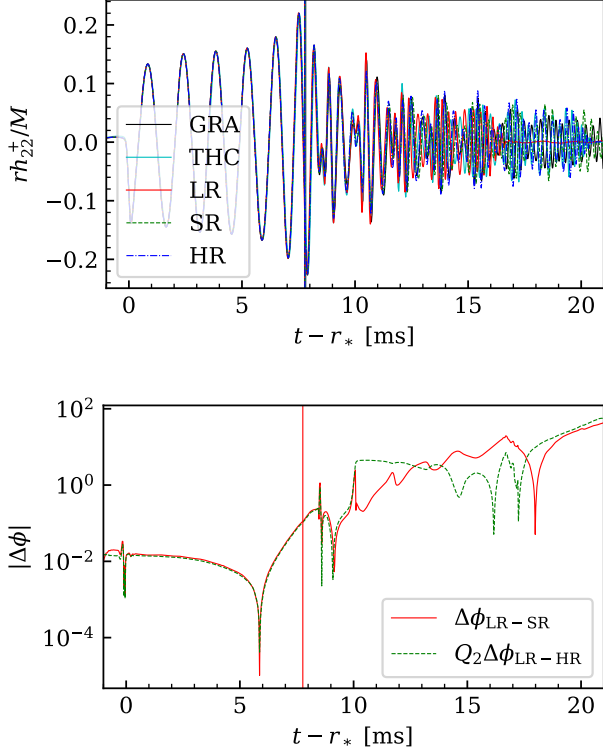


Figure 15. (Top) The real part of the gravitational wave strain in the $(2, 2)$ mode, normalized by extraction radius and gravitational mass. We compare our LR, SR, and HR **AthenaK** runs to a comparable run in **GR-Athena++**. Vertical lines show merger time as estimated by the peak amplitude of h_{22}^+ . (Bottom) Phase convergence of the three **AthenaK** runs. The difference between ϕ_{LR} and ϕ_{HR} is rescaled by a factor Q_2 assuming second-order convergence.

Most et al. 2019; Zappa et al. 2023). Though going to higher resolution may improve convergence, achieving second-order convergence is unlikely due to the presence of fluid turbulence, which, without including an explicit viscous term, will cascade to smaller length scales as resolution is increased.

As suggested by Figure 15, Figure 16 confirms that **AthenaK** agrees very well in the instantaneous frequency, $\omega_{22} = \dot{\phi}_{22}$, with both **GR-Athena++** and **WhiskyTHC** through merger. The reported frequencies at merger are $\omega_{22}^{\text{GRA}} \approx 1389$ Hz, $\omega_{22}^{\text{THC}} \approx 1329$ Hz, $\omega_{22}^{\text{LR}} \approx 1377$ Hz, $\omega_{22}^{\text{SR}} \approx 1359$ Hz, and $\omega_{22}^{\text{HR}} \approx 1353$ Hz, which are all consistent with each other.

We next consider the reduced binding energy, $E_b = (M_{\text{ADM}} - E_{\text{GW}} - M)/(M\nu)$, as a function of the reduced angular momentum, $j = (J_{\text{ADM}} - J_{\text{GW}})/(M^2\nu)$, where for our initial data $M_{\text{ADM}} = 2.9984 M_{\odot}$, $J_{\text{ADM}} = 8.83542 M_{\odot}^2$ in natural units, and the symmetric mass ratio is $\nu = q/(1+q)^2 = 1/4$. This is a gauge-invariant

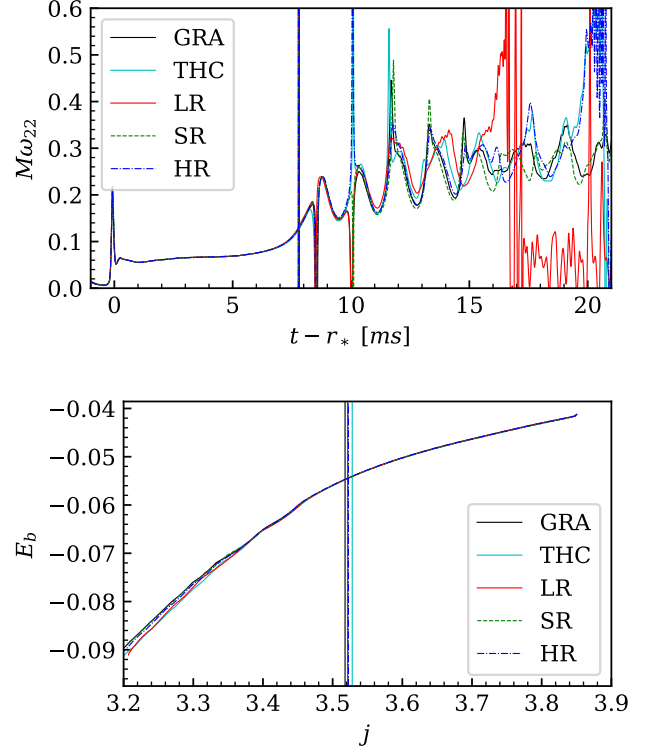


Figure 16. (Top) Instantaneous frequency of the $(2, 2)$ mode, ω_{22} , for **GR-Athena++** and the **AthenaK** runs. (Bottom) A plot of the reduced binding energy E_b and reduced angular momentum j . In both plots, vertical lines indicate merger times for each model.

measure which shows the evolution of the binary as it loses both energy and angular momentum due to gravitational radiation (Damour et al. 2012; Bernuzzi et al. 2012a). The bottom plot in Figure 16 shows that our runs are all in excellent agreement prior to merger. The lines do diverge somewhat in the post-merger phase, but the differences in the **AthenaK** runs decrease with resolution, indicating some measure of convergence.

Due to the effects of round-off error and the artificial atmosphere, mass will not be perfectly conserved in GRMHD evolutions. Figure 17 shows the mass conservation of BNS runs in **AthenaK** compared to **GR-Athena++**. Prior to merger, **AthenaK** demonstrates violations in mass conservation at $\sim 10^{-11}$ or better. Though the sign of this error changes, the magnitude of conservation violation remains at roughly this same order after merger until collapse for the LR case. This represents an improvement in conservation of $\mathcal{O}(10^4)$ or better over **GR-Athena++**. The SR and HR cases do begin to demonstrate large mass losses several milliseconds after merger. These errors, however, are simply due to

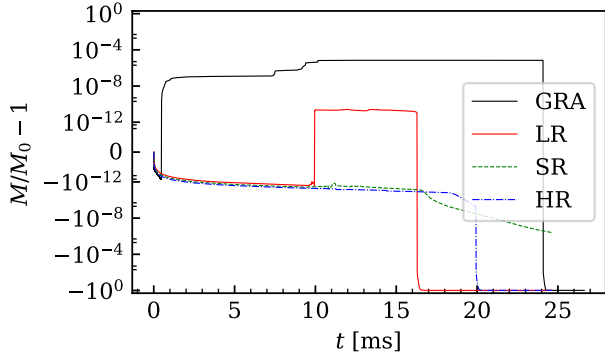


Figure 17. Mass conservation of AthenaK BNS runs compared to GR-Athena++.

matter outflows passing the edge of the computational domain.

Mass violations prior to merger seem to scale linearly with t , suggesting there is a small but consistent mass loss. This cannot be blamed on primitive inversion failures, as there are exactly two failures across all three runs (both of which occurred early in the HR run at points very close to atmosphere). We also cannot blame this on our flooring policy, which almost always results in an *increase* in mass. Though floating-point errors typically scale as \sqrt{t} , this is based on the assumption that floating-point errors are equally likely to round up as they are to round down. If such errors were instead consistently biased downward, the behavior would be approximately linear instead. One possibility leading to linear behavior may be truncation errors caused by mass fluxes between the atmosphere and the stellar surface or its outflows. However, we do not have sufficient evidence to confirm that this is the case.

5. SCALING AND PERFORMANCE

To evaluate the performance of AthenaK at large scales, we perform weak and strong scaling tests on OLCF Frontier, which has four AMD MI250X per node (each with two compute dies, or eight logical GPUs per node). Because scaling is highly problem-dependent, we provide two different test problems.

The first test problem tests only the Valencia GRMHD solver on a uniform grid in a fixed spacetime in a setup designed to explore the growth of turbulence, particularly the magnetorotational instability. The initial data is a Fishbone-Moncrief torus around a Kerr black hole with dimensionless spin $a = 0.9375$, similar to our setup used in Section 4.6. We zoom into a small cube located of width $\sim (M/M_\odot)$ km centered on $x = 9M$, $y = z = 0$ and fix the spacetime to the appropriate Kerr-Schild data. The strong scaling test has 8192 cells per

dimension for a resolution of $\Delta x \approx (M/M_\odot) 11.9$ cm, which requires a minimum of 1024 nodes. To perform weak scaling tests starting at a single node, we reduce the resolution to $1024 \times 1024 \times 512$ cells.

The second test problem consists of a single unperturbed TOV star in a dynamical spacetime similar to Section 4.5. To better emulate a typical BNS post-merger setup, we place it on an extended grid spanning $[-1024 M_\odot, 1024 M_\odot]$ in all directions with a base resolution of 256^3 points and six levels of refinement, with each successively halving the size of the domain. Therefore, the finest level has a resolution of $0.125 M_\odot$ (~ 185 m) on a region spanning $[-16 M_\odot, 16 M_\odot]$ in all directions, comparable in resolution to the SR run in 4.7.

For all tests, we use RK3, HLLE, and WENOZ, and we additionally enable FOFC for the turbulence setup but leave it disabled in the TOV/BNS setup (which incurs roughly a 3% to 5% performance decrease in our TOV tests above). We also disable all file output and diagnostic calculations, including wave extraction. Each test runs for 20 time steps, and performance is measured in terms of zone-cycles (or cell updates) per second.

5.1. Weak Scaling

In a weak scaling test, the problem size per node is kept fixed, i.e., resolution is increased to match computing resources. This measures the ability of a code to perform large-scale calculations before parallel communication becomes excessive. For each iteration of the test, we double the resolution in one dimension as the number of nodes is doubled. The turbulence test uses mesh blocks with 256^3 cells to maximize performance, but the TOV uses smaller mesh blocks of 64^3 cells to maintain the appropriate grid structure. We show results up to 65,536 GPUs (8192 nodes) in Figure 18. The turbulence setup maintains $\geq 87\%$ efficiency up to 65,536 GPUs, and the TOV setup maintains $\geq 81\%$ efficiency up to 32,768 GPUs and $\geq 74\%$ efficiency up to 65,536 GPUs.

The turbulence setup is ~ 4 times faster than the TOV setup. Profiling the code suggests that the Z4c solver is slightly slower than the GRMHD solver, which accounts for more than half of the slowdown. The mesh refinement, particularly the high-order prolongation and restriction operators, incur an additional performance penalty.

The remaining performance difference is related to the size of the mesh blocks. Smaller mesh blocks offer better flexibility for block-based SMR and AMR, but larger mesh blocks generally have improved performance. This occurs for two reasons: firstly, fewer mesh blocks means

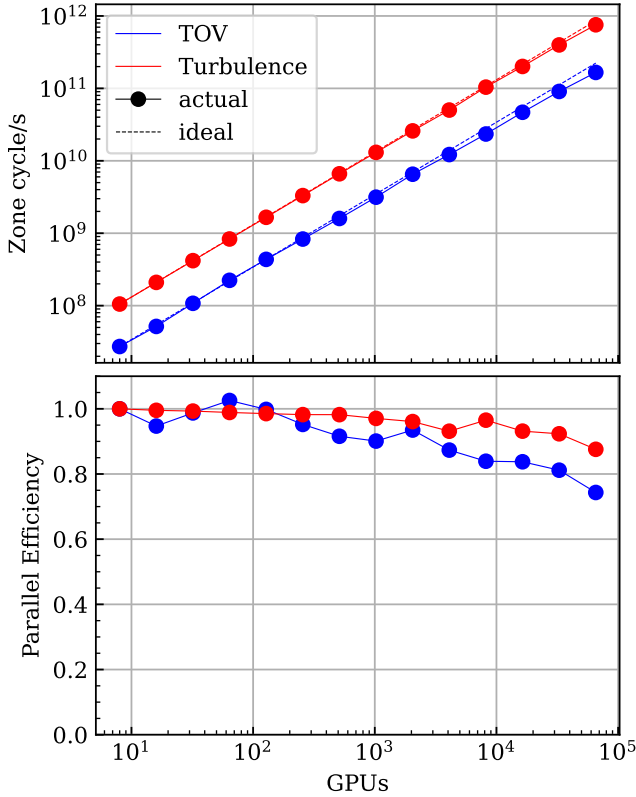


Figure 18. Weak scaling results of a single neutron star (blue) and a turbulence setup (red) on OLCF Frontier. The top plot displays raw performance (solid lines) in terms of zone-cycles per second relative to ideal scaling (dashed lines). The bottom plot shows parallel efficiency relative to a single node as a function of GPU count.

less interblock communication as there are fewer ghost cells relative to the number of physical cells. Secondly (and more importantly), the innermost level of vectorization in the GRMHD solver operates on single lines in the x direction. This is convenient for reconstruction operators, which are most easily written to reconstruct one side of two different interfaces, and it generally offers better CPU performance. However, GPU performance becomes very closely tied to the length of the mesh block in the x direction as a result. Consequently, the larger mesh blocks in the turbulence test offer a modest performance boost over the smaller blocks used in the TOV test.

5.2. Strong Scaling

Strong scaling measures how increasing computational resources speeds up the calculation of a fixed problem size. Though strong scaling does demonstrate the effects of increased communication overhead, it also measures how large of a problem is needed to achieve optimal performance. A GPU requires relatively heavy workloads

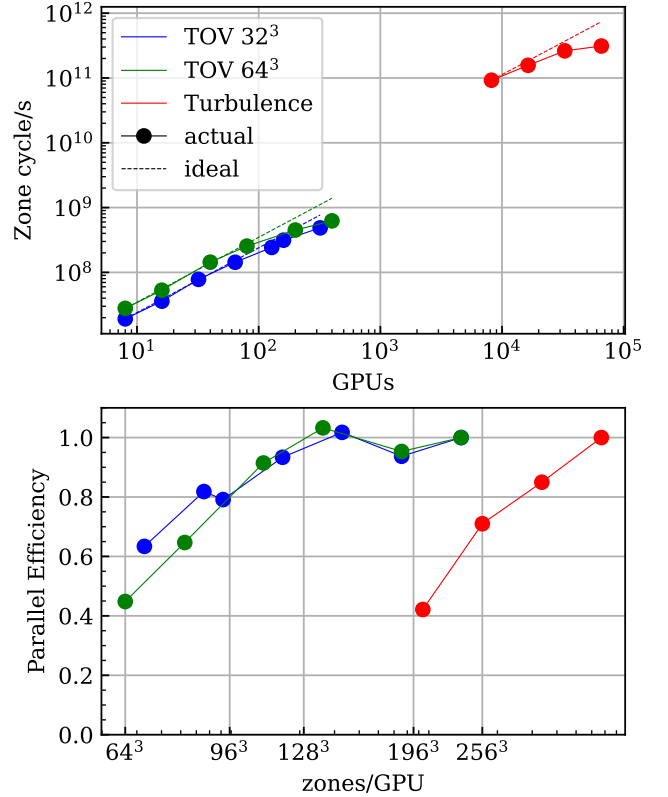


Figure 19. The same as Figure 18, but for strong scaling instead, and with efficiency measured against zones per GPU rather than total GPU count.

both to saturate the device and to negate the overhead of launching a new kernel. However, GPUs generally contain far less memory per TFLOP than CPU-based machines; this makes strong scaling tests more difficult on GPUs, as there is less difference between a saturating workload and the maximum possible workload.

For the TOV test, we perform tests with mesh block sizes of 32^3 and 64^3 . As mentioned above, the mesh block size is closely related to the performance of the GRMHD solver, so these two tests provide a way to quantify this effect in configurations suitable for a BNS remnant. The turbulence test is done with a single configuration using mesh blocks of 128^3 each, which offers marginally worse performance ($< 1\%$ decrease) than the larger mesh blocks used in Section 5.1, but it allows us to scale to larger node counts.

We show the strong-scaling test results in Figure 19. Relative to a single node ($\sim 236^3$ zones per GPU), AthenaK on Frontier maintains $\geq 80\%$ efficiency down to $\sim 96^3$ zones per GPU for the TOV test. The 64^3 block test is roughly 45% faster than the 32^3 test, suggesting that 32^3 mesh blocks do not saturate the GPUs properly. Despite the performance difference, scaling results are comparable between the two setups at smaller

Table 2. Summary of AthenaK performance for a freely evolving TOV on different architectures. Speedup is measured relative to a single 64-core CPU socket on an AMD EPYC 7763. For reference, **GR-Athena++** results on this system are also included.

Architecture	10^6 zone-cycles/s	Speedup
EPYC 7763	0.760	1
EPYC 7763 (GR-Athena++)	0.964	1.27
A100	10.7	14.1
MI250X	4.84	6.37
Ryzen 9 5900X	0.125	0.164
RTX 3070 (laptop)	1.08	1.42

node counts. However, there is some evidence suggesting that large mesh blocks scale more poorly at large node counts. Though the limited tests shown here are hardly conclusive, this seems reasonable; larger mesh blocks improve GPU vectorization and reduce the total number of communication calls, but the cost of launching a kernel does not substantially change, meaning that kernel overhead will become a bottleneck sooner than in the case of small mesh blocks.

Strong scaling for the turbulence test is not as good, with efficiency decreasing to 71% after only quadrupling the number of resources (going from $\sim 406^3$ to $\sim 256^3$ zones per GPU). This is not unexpected, as this test lacks both the Z4c solver and the computational overhead associated with mesh refinement.

5.3. Discussion on Performance

Our scaling results are best compared to **Parthenon**, a similar Kokkos-based AMR framework derived from **Athena++** (Grete et al. 2023). Our turbulence weak scaling results are similar to those reported for **Parthenon** on Frontier. We cannot draw a direct comparison for the TOV tests, as **Parthenon** does not have weak scaling results for its mesh refinement. Strong scaling is noticeably poorer in all cases considered, but a likely explanation for this is the additional memory footprint required by our tests limiting the size of the tests we can run; compared to standard hydrodynamics, which need only store the conserved and primitive variables, MHD requires additional memory for both the face and cell-centered magnetic fields. The GRMHD implementation presented here also stores the ADM variables to support generic spacetimes, even when such spacetimes are unevolved. Therefore, they consume significant memory but do not contribute to the overall computational load.

In addition to the scaling results above, we performed a small number of tests comparing CPU and GPU performance on NERSC Perlmutter, which consists of CPU

nodes (each with two AMD EPYC 7763 CPUs) and GPU nodes (each with a single CPU and four Nvidia A100 GPUs). Our setup is similar to Sec. 4.5 but with all output disabled and limited to the first 20 time steps. We also reduce the resolution to 128^3 with mesh blocks of size 32^3 to ensure they fit on a single 40 GB GPU. Running with a single CPU (64 cores/128 threads) achieves 7.60×10^5 zone-cycles/s, and a single Nvidia A100 GPU manages to achieve 1.07×10^7 zone-cycles/s, a factor of ~ 14 improvement. The same setup on OLCF Frontier using a single MI250X compute die achieves 4.84×10^6 zone-cycles/s. To provide a baseline comparison, we also perform this test with **GR-Athena++** using as similar a setup as possible. For a cell-centered space-time, **GR-Athena++** achieves 9.64×10^5 zone-cycles/s, which is somewhat faster but comparable to **AthenaK**'s CPU performance.

We also ran a version of this test on a consumer-grade laptop with an Nvidia RTX 3070 laptop GPU. Due to the reduced amount of memory, we reduced the resolution by half, switched to 16^3 mesh blocks, and imposed a reflection symmetry across the z-axis, but the physics options are the same. The laptop GPU achieves 1.08×10^6 zone-cycles/s, which is 42% faster than a single CPU on Perlmutter. The same calculation using the laptop's CPU (an AMD Ryzen 9 5900X) with 16 OpenMP threads only achieved 1.25×10^5 zone-cycles/s. All of these results are summarized in Table 2. We also found it possible to run a very coarse (~ 900 m) BNS simulation through merger on this same device in a matter of a few hours. Though research-grade calculations still require larger machines, the order-of-magnitude speedup provided by GPUs makes it possible to accelerate testing and debugging considerably.

6. CONCLUSION

In this paper, we have introduced an extension to **AthenaK**'s GRMHD capabilities to dynamical spacetimes. Our solver uses the Valencia formulation and finite-volume methods, and we incorporate an FOFC scheme with optional DMP enforcement to improve our atmosphere treatment enhance overall stability.

We have performed a number of standard tests in both flat and curved spacetimes. **AthenaK** is in excellent agreement with analytical results where they exist and compares favorably with other GRMHD codes. In particular, our cylindrical blast wave test demonstrates the ability of the FOFC scheme to improve robustness when handling strongly magnetized flows, which enables us to evolve a strongly magnetized blast wave with WENOZ. We also accurately reproduce the oscillation frequencies of a TOV star in both the Cowling approximation and

full GR, and we show that the FOFC scheme does not adversely affect this evolution.

To validate **AthenaK**'s magnetic field evolution in curved spacetimes, we compare the results of a SANE accretion disk around a Kerr black hole to several of the GRMHD codes in the EHT code comparison project (Porth et al. 2019). **AthenaK** achieves similar results, validating the GRMHD solver on a highly nontrivial problem. This test also allows a consistent comparison between **AthenaK**'s standard HARM-like GRMHD solver and the new solver we have added for dynamical spacetimes based on the Valencia formulation. We find some small qualitative differences which may be due to their different energy terms. Nevertheless, these differences seem to be minor, and the comparison with other GRMHD codes suggests that one's choice of numerical methods and grid structure have a far larger effect on the evolution.

We also perform unmagnetized BNS simulations on GPUs, which reproduce the results shown in (Cook et al. 2023) with **GR-Athena++** and are in excellent agreement with **WhiskyTHC**. A resolution study shows that **AthenaK**'s gravitational waves achieve second-order phase convergence, and we are able to evolve stably through collapse. Thanks to the FOFC scheme, we also show that **AthenaK** improves mass conservation over **GR-Athena++** by a factor of $\mathcal{O}(10^4)$.

The performance of **AthenaK** is also very good, with GPUs demonstrating an order-of-magnitude speedup over CPUs. We also only demonstrate a small slowdown on CPUs relative to a cell-centered version of **GR-Athena++** despite optimizing our vectorization for GPU performance. We maintain 74% weak scaling efficiency up to 65,536 GPUs and better than 80% up to 32,768 GPUs on OLCF Frontier for a dynamical GRMHD problem. We also maintain better than 70% strong scaling efficiency down to $\sim 96^3$ cells per GPU, which corresponds to less than 4 64^3 mesh blocks or 27 32^3 mesh blocks per GPU. Our fixed-spacetime turbulence tests achieve better than 87% efficiency weak efficiency up to 65,536 GPUs.

We are also working to expand **AthenaK**'s physics capabilities. Microphysical tabulated equations of state are being tested, and we are also developing a new neu-

trino transport module based on a finite-element scheme (Bhattacharyya & Radice 2022). Nevertheless, even without these enhancements, **AthenaK**'s exascale-ready performance and excellent stability properties make it a capable tool for NR applications such as precision waveform modeling.

1 The authors thank the Penn State Numerical Relativity
2 Group for helpful discussions and important feedback.
3 This research makes use of data from the EHT Code
4 Comparison Project, and JF thanks Oliver Porth for
5 assistance with accessing the data.

6 Part of this work was completed at the TACC Open
7 Hackathon, part of the Open Hackathons program.
8 The authors would like to acknowledge OpenACC-
9 Standard.org for their support. We are particularly
10 grateful to Matthew Cawood, Victor Eijkhout, and
11 Forrest Glines for helpful discussions while optimizing
12 **AthenaK**.

13 SB and BD acknowledge support by the EU Hori-
14 zon under ERC Consolidator Grant, no. InspiReM-
15 101043372.

16 This research was supported by funding from the
17 U.S. Department of Energy, Office of Science, Divi-
18 sion of Nuclear Physics under Award Number(s) DE-
19 SC0021177 and DE-SC0024388, by NASA under award
20 No. 80NSSC21K1720, and by the National Science
21 Foundation under Grants No. PHY-2011725, PHY-
22 2020275, PHY-2116686, and AST-2108467.

23 Part of this work was completed during a sabbatical
24 visit to the Institute for Gravitation and the Cosmos at
25 the Pennsylvania State University by SB.

26 Simulations were performed on OLCF's Frontier,
27 NERSC's Perlmutter, and on the Pennsylvania State
28 University's Institute for Computational and Data Sci-
29 ences's Roar Collab supercomputer. This research used
30 resources of the National Energy Research Scientific
31 Computing Center, a DOE Office of Science User Facil-
32 ity supported by the Office of Science of the U.S. De-
33 partment of Energy under Contract No. DE-AC02-
34 05CH11231. This research used resources of the Oak
35 Ridge Leadership Computing Facility at the Oak Ridge
36 National Laboratory, which is supported by the Office
37 of Science of the U.S. Department of Energy under Con-
38 tract No. DE-AC05-00OR22725.

REFERENCES

- Abbott, B. P., et al. 2016, *Phys. Rev. Lett.*, 116, 061102,
doi: [10.1103/PhysRevLett.116.061102](https://doi.org/10.1103/PhysRevLett.116.061102)
- . 2017a, *Phys. Rev. Lett.*, 119, 161101,
doi: [10.1103/PhysRevLett.119.161101](https://doi.org/10.1103/PhysRevLett.119.161101)
- . 2017b, *Class. Quant. Grav.*, 34, 044001,
doi: [10.1088/1361-6382/aa51f4](https://doi.org/10.1088/1361-6382/aa51f4)
- Anninos, P., Fragile, P. C., & Salmonson, J. D. 2005,
Astrophys. J., 635, 723, doi: [10.1086/497294](https://doi.org/10.1086/497294)

- Anton, L., Zanotti, O., Miralles, J. A., et al. 2006, *Astrophys. J.*, 637, 296, doi: [10.1086/498238](https://doi.org/10.1086/498238)
- Balsara, D. 2001, *The Astrophysical Journal Supplement Series*, 132, 83, doi: [10.1086/318941](https://doi.org/10.1086/318941)
- Banyuls, F., Font, J. A., Ibáñez, J. M., Martí, J. M., & Miralles, J. A. 1997, *ApJ*, 476, 221, doi: [10.1086/303604](https://doi.org/10.1086/303604)
- Beckwith, K., & Stone, J. M. 2011, *Astrophys. J. Suppl.*, 193, 6, doi: [10.1088/0067-0049/193/1/6](https://doi.org/10.1088/0067-0049/193/1/6)
- Berger, M. J., & Olinger, J. 1984, *J. Comput. Phys.*, 53, 484, doi: [10.1016/0021-9991\(84\)90073-1](https://doi.org/10.1016/0021-9991(84)90073-1)
- Bernuzzi, S., & Hilditch, D. 2010, *Phys. Rev. D*, 81, 084003, doi: [10.1103/PhysRevD.81.084003](https://doi.org/10.1103/PhysRevD.81.084003)
- Bernuzzi, S., Nagar, A., Thierfelder, M., & Bruggmann, B. 2012a, *Phys. Rev. D*, 86, 044030, doi: [10.1103/PhysRevD.86.044030](https://doi.org/10.1103/PhysRevD.86.044030)
- Bernuzzi, S., Thierfelder, M., & Bruggmann, B. 2012b, *Phys. Rev. D*, 85, 104030, doi: [10.1103/PhysRevD.85.104030](https://doi.org/10.1103/PhysRevD.85.104030)
- Bhattacharyya, M. K., & Radice, D. 2022, doi: [10.1016/j.jcp.2023.112365](https://doi.org/10.1016/j.jcp.2023.112365)
- Borges, R., Carmona, M., Costa, B., & Don, W. S. 2008, *J. of Comp. Phys.*, 227, 3191, doi: [10.1016/j.jcp.2007.11.038](https://doi.org/10.1016/j.jcp.2007.11.038)
- Boyle, M., Buonanno, A., Kidder, L. E., et al. 2008, *Phys. Rev. D*, 78, 104020, doi: [10.1103/PhysRevD.78.104020](https://doi.org/10.1103/PhysRevD.78.104020)
- Brandt, S. R., Haas, R., Diener, P., et al. 2024, *The Einstein Toolkit, The "Lev Landau" release, ET_2024.05*, Zenodo, doi: [10.5281/zenodo.12588764](https://doi.org/10.5281/zenodo.12588764)
- Bugner, M., Dietrich, T., Bernuzzi, S., Weyhausen, A., & Brüggmann, B. 2016, *Phys. Rev. D*, 94, 084004, doi: [10.1103/PhysRevD.94.084004](https://doi.org/10.1103/PhysRevD.94.084004)
- Clain, S., Diot, S., & Loubère, R. 2011, *Journal of Computational Physics*, 230, 4028, doi: <https://doi.org/10.1016/j.jcp.2011.02.026>
- Clough, K., Figueras, P., Finkel, H., et al. 2015, *Class. Quant. Grav.*, 32, 245011, doi: [10.1088/0264-9381/32/24/245011](https://doi.org/10.1088/0264-9381/32/24/245011)
- Colella, P., & Sekora, M. D. 2008, *J. of Comp. Phys.*, 227, 7069, doi: [10.1016/j.jcp.2008.03.034](https://doi.org/10.1016/j.jcp.2008.03.034)
- Colella, P., & Woodward, P. R. 1984, *J. of Comp. Phys.*, 54, 174, doi: [10.1016/0021-9991\(84\)90143-8](https://doi.org/10.1016/0021-9991(84)90143-8)
- Cook, W., Daszuta, B., Fields, J., et al. 2023, <https://arxiv.org/abs/2311.04989>
- Damour, T., Nagar, A., Pollney, D., & Reisswig, C. 2012, *Phys. Rev. Lett.*, 108, 131101, doi: [10.1103/PhysRevLett.108.131101](https://doi.org/10.1103/PhysRevLett.108.131101)
- Daszuta, B., Cook, W., Hammond, P., et al. 2024, <https://arxiv.org/abs/2406.09139>
- Daszuta, B., Zappa, F., Cook, W., et al. 2021, *Astrophys. J. Suppl.*, 257, 25, doi: [10.3847/1538-4365/ac157b](https://doi.org/10.3847/1538-4365/ac157b)
- Del Zanna, L., Zanotti, O., Bucciantini, N., & Londrillo, P. 2007, *Astron. Astrophys.*, 473, 11, doi: [10.1051/0004-6361:20077093](https://doi.org/10.1051/0004-6361:20077093)
- Deppe, N., Kidder, L. E., Teukolsky, S. A., et al. 2023, *Class. Quant. Grav.*, 40, 245014, doi: [10.1088/1361-6382/ad08f7](https://doi.org/10.1088/1361-6382/ad08f7)
- DeVore, C. 1991, *Journal of Computational Physics*, 92, 142, doi: [https://doi.org/10.1016/0021-9991\(91\)90295-V](https://doi.org/10.1016/0021-9991(91)90295-V)
- Einfeldt, B., Munz, C., Roe, P., & Sjögren, B. 1991, *J. of Comp. Phys.*, 92, 273, doi: [https://doi.org/10.1016/0021-9991\(91\)90211-3](https://doi.org/10.1016/0021-9991(91)90211-3)
- Espino, P. L., Bozzola, G., & Paschalidis, V. 2023, *Phys. Rev. D*, 107, 104059, doi: [10.1103/PhysRevD.107.104059](https://doi.org/10.1103/PhysRevD.107.104059)
- Etienne, Z. B., Paschalidis, V., Haas, R., Mösta, P., & Shapiro, S. L. 2015, *Class. Quant. Grav.*, 32, 175009, doi: [10.1088/0264-9381/32/17/175009](https://doi.org/10.1088/0264-9381/32/17/175009)
- Fernando, M., Neilsen, D., Hirschmann, E., et al. 2022, in *Super Computing 2022* (IEEE Press), 1078–1092
- Fernando, M., Neilsen, D., Lim, H., Hirschmann, E., & Sundar, H. 2019, *SIAM J. Sci. Comput.*, 41, C97, doi: [10.1137/18M1196972](https://doi.org/10.1137/18M1196972)
- Fernando, M., Neilsen, D., Zlochower, Y., Hirschmann, E. W., & Sundar, H. 2023, *Phys. Rev. D*, 107, 064035, doi: [10.1103/PhysRevD.107.064035](https://doi.org/10.1103/PhysRevD.107.064035)
- Fishbone, L. G., & Moncrief, V. 1976, *ApJ*, 207, 962, doi: [10.1086/154565](https://doi.org/10.1086/154565)
- Foucart, F., Duez, M. D., Hebert, F., et al. 2021, *Astrophys. J.*, 920, 82, doi: [10.3847/1538-4357/ac1737](https://doi.org/10.3847/1538-4357/ac1737)
- Fragile, P. C., Gillespie, A., Monahan, T., Rodriguez, M., & Anninos, P. 2012, *ApJS*, 201, 9, doi: [10.1088/0067-0049/201/2/9](https://doi.org/10.1088/0067-0049/201/2/9)
- Fragile, P. C., Olejar, A., & Anninos, P. 2014, *Astrophys. J.*, 796, 22, doi: [10.1088/0004-637X/796/1/22](https://doi.org/10.1088/0004-637X/796/1/22)
- Gamba, R., Breschi, M., Bernuzzi, S., Agathos, M., & Nagar, A. 2021, *Phys. Rev. D*, 103, 124015, doi: [10.1103/PhysRevD.103.124015](https://doi.org/10.1103/PhysRevD.103.124015)
- Gammie, C. F., McKinney, J. C., & Toth, G. 2003, *Astrophys. J.*, 589, 444, doi: [10.1086/374594](https://doi.org/10.1086/374594)
- Gardiner, T. A., & Stone, J. M. 2005, *J. Comput. Phys.*, 205, 509, doi: [10.1016/j.jcp.2004.11.016](https://doi.org/10.1016/j.jcp.2004.11.016)
- . 2008, *J. Comput. Phys.*, 227, 4123, doi: [10.1016/j.jcp.2007.12.017](https://doi.org/10.1016/j.jcp.2007.12.017)
- Giacomazzo, B., & Rezzolla, L. 2006, *J. Fluid Mech.*, 562, 223, doi: [10.1017/S0022112006001145](https://doi.org/10.1017/S0022112006001145)
- . 2007, *Class. Quant. Grav.*, 24, S235, doi: [10.1088/0264-9381/24/12/S16](https://doi.org/10.1088/0264-9381/24/12/S16)
- Giacomazzo, B., Rezzolla, L., & Baiotti, L. 2009, *Mon. Not. Roy. Astron. Soc.*, 399, L164, doi: [10.1111/j.1745-3933.2009.00745.x](https://doi.org/10.1111/j.1745-3933.2009.00745.x)

- Gottlieb, S., Ketcheson, D. I., & Shu, C.-W. 2009, *J. Sci. Comput.*, 38, 251, doi: [10.1007/s10915-008-9239-z](https://doi.org/10.1007/s10915-008-9239-z)
- Gourgoulhon, E., Grandclément, P., Marck, J.-A., Novak, J., & Taniguchi, K. 2016, LORENE: Spectral methods differential equations solver, *Astrophysics Source Code Library*, record ascl:1608.018. <http://ascl.net/1608.018>
- Gourgoulhon, E., Grandclément, P., Taniguchi, K., Marck, J.-A., & Bonazzola, S. 2001, *Phys. Rev. D*, 63, 064029, doi: [10.1103/PhysRevD.63.064029](https://doi.org/10.1103/PhysRevD.63.064029)
- Grete, P., Dolence, J. C., Miller, J. M., et al. 2023, *The International Journal of High Performance Computing Applications*, 37, 465, doi: [10.1177/10943420221143775](https://doi.org/10.1177/10943420221143775)
- Harten, A., Lax, P. D., & Leer, B. v. 1983, *SIAM Review*, 25, 35, doi: [10.1137/1025002](https://doi.org/10.1137/1025002)
- Hilditch, D., Bernuzzi, S., Thierfelder, M., et al. 2013, *Phys. Rev. D*, 88, 084057, doi: [10.1103/PhysRevD.88.084057](https://doi.org/10.1103/PhysRevD.88.084057)
- Hilditch, D., Weyhausen, A., & Brüggmann, B. 2016, *Phys. Rev. D*, 93, 063006, doi: [10.1103/PhysRevD.93.063006](https://doi.org/10.1103/PhysRevD.93.063006)
- Hinderer, T., et al. 2019, *Phys. Rev. D*, 100, 06321, doi: [10.1103/PhysRevD.100.06321](https://doi.org/10.1103/PhysRevD.100.06321)
- Ioka, K., & Taniguchi, K. 2000, *Astrophys. J.*, 537, 327, doi: [10.1086/309004](https://doi.org/10.1086/309004)
- Izquierdo, M. R., Pareschi, L., Miñano, B., Massó, J., & Palenzuela, C. 2023, *Class. Quant. Grav.*, 40, 145014, doi: [10.1088/1361-6382/acd97f](https://doi.org/10.1088/1361-6382/acd97f)
- Kalinani, J. V., et al. 2024. <https://arxiv.org/abs/2406.11669>
- Kastaun, W. 2021, wokast/RePrimAnd: Version 1.3, v1.3, Zenodo, doi: [10.5281/zenodo.5136386](https://doi.org/10.5281/zenodo.5136386)
- Kastaun, W., Kalinani, J. V., & Ciolfi, R. 2021, *Phys. Rev. D*, 103, 023018, doi: [10.1103/PhysRevD.103.023018](https://doi.org/10.1103/PhysRevD.103.023018)
- Kidder, L. E., et al. 2017, *J. Comput. Phys.*, 335, 84, doi: [10.1016/j.jcp.2016.12.059](https://doi.org/10.1016/j.jcp.2016.12.059)
- Kiuchi, K., Held, L. E., Sekiguchi, Y., & Shibata, M. 2022, *Phys. Rev. D*, 106, 124041, doi: [10.1103/PhysRevD.106.124041](https://doi.org/10.1103/PhysRevD.106.124041)
- Komissarov, S., & Phillips, D. 2024. <https://arxiv.org/abs/2409.03637>
- Komissarov, S. S. 1999, *Mon. Not. R. Astron. Soc.*, 303, 343, doi: [10.1046/j.1365-8711.1999.02244.x](https://doi.org/10.1046/j.1365-8711.1999.02244.x)
- Kružkov, S. N. 1970, *Mathematics of the USSR-Sbornik*, 10, 217, doi: [10.1070/SM1970v010n02ABEH002156](https://doi.org/10.1070/SM1970v010n02ABEH002156)
- Leismann, T., Antón, L., Aloy, M. A., et al. 2005, *A&A*, 436, 503, doi: [10.1051/0004-6361:20042520](https://doi.org/10.1051/0004-6361:20042520)
- Lemaster, M. N., & Stone, J. M. 2009, *Astrophys. J.*, 691, 1092, doi: [10.1088/0004-637X/691/2/1092](https://doi.org/10.1088/0004-637X/691/2/1092)
- Loffler, F., et al. 2012, *Class. Quant. Grav.*, 29, 115001, doi: [10.1088/0264-9381/29/11/115001](https://doi.org/10.1088/0264-9381/29/11/115001)
- Maggiore, M., et al. 2020, *JCAP*, 2020, 050, doi: [10.1088/1475-7516/2020/03/050](https://doi.org/10.1088/1475-7516/2020/03/050)
- McKinney, J. C., & Gammie, C. F. 2004, *Astrophys. J.*, 611, 977, doi: [10.1086/422244](https://doi.org/10.1086/422244)
- Mignone, A., & Bodo, G. 2006, *Mon. Not. Roy. Astron. Soc.*, 368, 1040, doi: [10.1111/j.1365-2966.2006.10162.x](https://doi.org/10.1111/j.1365-2966.2006.10162.x)
- Most, E. R., Papenfort, L. J., & Rezzolla, L. 2019, *Mon. Not. Roy. Astron. Soc.*, 490, 3588, doi: [10.1093/mnras/stz2809](https://doi.org/10.1093/mnras/stz2809)
- Noble, S. C., & Choptuik, M. W. 2008, *Phys. Rev. D*, 78, 064059, doi: [10.1103/PhysRevD.78.064059](https://doi.org/10.1103/PhysRevD.78.064059)
- Noble, S. C., Gammie, C. F., McKinney, J. C., & Del Zanna, L. 2006, *Astrophys. J.*, 641, 626, doi: [10.1086/500349](https://doi.org/10.1086/500349)
- Noble, S. C., Krolik, J. H., & Hawley, J. F. 2009, *Astrophys. J.*, 692, 411, doi: [10.1088/0004-637X/692/1/411](https://doi.org/10.1088/0004-637X/692/1/411)
- Novak, J. 2001, *Astron. Astrophys.*, 376, 606, doi: [10.1051/0004-6361:20011037](https://doi.org/10.1051/0004-6361:20011037)
- Palenzuela, C., Liebling, S., & Miñano, B. 2022, *Phys. Rev. D*, 105, 103020, doi: [10.1103/PhysRevD.105.103020](https://doi.org/10.1103/PhysRevD.105.103020)
- Palenzuela, C., Liebling, S. L., Neilsen, D., et al. 2015, *Phys. Rev. D*, 92, 044045, doi: [10.1103/PhysRevD.92.044045](https://doi.org/10.1103/PhysRevD.92.044045)
- Phillips, D., & Komissarov, S. 2024, *J. Phys. Conf. Ser.*, 2742, 012018, doi: [10.1088/1742-6596/2742/1/012018](https://doi.org/10.1088/1742-6596/2742/1/012018)
- Pollney, D., Reisswig, C., Schnetter, E., Dorband, N., & Diener, P. 2011, *Phys. Rev. D*, 83, 044045, doi: [10.1103/PhysRevD.83.044045](https://doi.org/10.1103/PhysRevD.83.044045)
- Porth, O., Olivares, H., Mizuno, Y., et al. 2017, *Comput. Astrophys. Cosmol.*, 4, 1, doi: [10.1186/s40668-017-0020-2](https://doi.org/10.1186/s40668-017-0020-2)
- Porth, O., et al. 2019, *Astrophys. J. Suppl.*, 243, 26, doi: [10.3847/1538-4365/ab29fd](https://doi.org/10.3847/1538-4365/ab29fd)
- Poudel, A., Tichy, W., Brüggmann, B., & Dietrich, T. 2020, *Phys. Rev. D*, 102, 104014, doi: [10.1103/PhysRevD.102.104014](https://doi.org/10.1103/PhysRevD.102.104014)
- Pürrer, M., & Haster, C.-J. 2020, *Phys. Rev. Res.*, 2, 023151, doi: [10.1103/PhysRevResearch.2.023151](https://doi.org/10.1103/PhysRevResearch.2.023151)
- Radia, M., Spherhake, U., Drew, A., et al. 2022, *Class. Quant. Grav.*, 39, 135006, doi: [10.1088/1361-6382/ac6fa9](https://doi.org/10.1088/1361-6382/ac6fa9)
- Radice, D., Bernuzzi, S., Perego, A., & Haas, R. 2022, *Mon. Not. Roy. Astron. Soc.*, 512, 1499, doi: [10.1093/mnras/stac589](https://doi.org/10.1093/mnras/stac589)
- Radice, D., Perego, A., Zappa, F., & Bernuzzi, S. 2018, *Astrophys. J. Lett.*, 852, L29, doi: [10.3847/2041-8213/aaa402](https://doi.org/10.3847/2041-8213/aaa402)
- Radice, D., & Rezzolla, L. 2012, *Astron. Astrophys.*, 547, A26, doi: [10.1051/0004-6361/201219735](https://doi.org/10.1051/0004-6361/201219735)
- Radice, D., Rezzolla, L., & Galeazzi, F. 2014a, *Class. Quant. Grav.*, 31, 075012, doi: [10.1088/0264-9381/31/7/075012](https://doi.org/10.1088/0264-9381/31/7/075012)
- . 2014b, *Mon. Not. Roy. Astron. Soc.*, 437, L46, doi: [10.1093/mnrasl/slt137](https://doi.org/10.1093/mnrasl/slt137)

- . 2015, ASP Conf. Ser., 498, 121.
<https://arxiv.org/abs/1502.00551>
- Rashti, A., Bhattacharyya, M., Radice, D., et al. 2024, *Class. Quant. Grav.*, 41, 095001, doi: [10.1088/1361-6382/ad36a5](https://doi.org/10.1088/1361-6382/ad36a5)
- Reisswig, C., Ott, C. D., Abdikamalov, E., et al. 2013, *Phys. Rev. Lett.*, 111, 151101, doi: [10.1103/PhysRevLett.111.151101](https://doi.org/10.1103/PhysRevLett.111.151101)
- Ruiz, M., Shapiro, S. L., & Tsokaros, A. 2018, *Phys. Rev. D*, 97, 021501, doi: [10.1103/PhysRevD.97.021501](https://doi.org/10.1103/PhysRevD.97.021501)
- Sadowski, A., Narayan, R., McKinney, J. C., & Tchekhovskoy, A. 2014, *Mon. Not. Roy. Astron. Soc.*, 439, 503, doi: [10.1093/mnras/stt2479](https://doi.org/10.1093/mnras/stt2479)
- Sadowski, A., Narayan, R., Tchekhovskoy, A., & Zhu, Y. 2013, *MNRAS*, 429, 3533, doi: [10.1093/mnras/sts632](https://doi.org/10.1093/mnras/sts632)
- Shankar, S., Mösta, P., Brandt, S. R., et al. 2023, *Class. Quant. Grav.*, 40, 205009, doi: [10.1088/1361-6382/acf2d9](https://doi.org/10.1088/1361-6382/acf2d9)
- Shibata, M., Fujibayashi, S., Hotokezaka, K., et al. 2017, *Phys. Rev. D*, 96, 123012, doi: [10.1103/PhysRevD.96.123012](https://doi.org/10.1103/PhysRevD.96.123012)
- Stergioulas, N., Apostolatos, T. A., & Font, J. A. 2004, *Mon. Not. Roy. Astron. Soc.*, 352, 1089, doi: [10.1111/j.1365-2966.2004.07973.x](https://doi.org/10.1111/j.1365-2966.2004.07973.x)
- Stone, J. M., Tomida, K., White, C. J., & Felker, K. G. 2020, *Astrophys. J. Suppl.*, 249, 4, doi: [10.3847/1538-4365/ab929b](https://doi.org/10.3847/1538-4365/ab929b)
- Stone, J. M., Mullen, P., Fielding, D., et al. 2024. <https://arxiv.org/abs/2409.16053>
- Tichy, W., Ji, L., Adhikari, A., Rashti, A., & Pirog, M. 2023, *Class. Quant. Grav.*, 40, 025004, doi: [10.1088/1361-6382/acaee7](https://doi.org/10.1088/1361-6382/acaee7)
- Trott, C. R., Lebrun-Grandié, D., Arndt, D., et al. 2022, *IEEE Transactions on Parallel and Distributed Systems*, 33, 805, doi: [10.1109/TPDS.2021.3097283](https://doi.org/10.1109/TPDS.2021.3097283)
- van Leer, B. 1974, *Journal of Computational Physics*, 14, 361, doi: [https://doi.org/10.1016/0021-9991\(74\)90019-9](https://doi.org/10.1016/0021-9991(74)90019-9)
- Yoshida, S., & Eriguchi, Y. 2001, *Mon. Not. Roy. Astron. Soc.*, 322, 389, doi: [10.1046/j.1365-8711.2001.04115.x](https://doi.org/10.1046/j.1365-8711.2001.04115.x)
- Zanotti, O., Fambri, F., & Dumbser, M. 2015, *Mon. Not. Roy. Astron. Soc.*, 452, 3010, doi: [10.1093/mnras/stv1510](https://doi.org/10.1093/mnras/stv1510)
- Zappa, F., Bernuzzi, S., Radice, D., & Perego, A. 2023, *Mon. Not. R. Astron. Soc.*, doi: [10.1093/mnras/stad107](https://doi.org/10.1093/mnras/stad107)
- Zhu, H., Fields, J., Zappa, F., et al. 2024. <https://arxiv.org/abs/2409.10383>